Geophysical Research Letters

RESEARCH LETTER
10.1029/2025GL118863

Key Points:

- Supershear rupture occurred during the 2025 M_w 7.8 Myanmar earthquake but did not propagate under steady-state conditions
- A negative fault-parallel secondary velocity pulse recorded at a near-fault strong motion station NPW indicates rupture stopping phase
- A fault barrier at ~6 km south of the NPW station can explain the identified stopping phase as supported by numerical simulations

Supporting Information:

Supporting Information may be found in the online version of this article.

Correspondence to:

S. Xu,
xusq3@sustech.edu.cn

Citation:

Ding, X., Xu, S., & Ye, L. (2025). Intermittent supershear rupture punctuated by barrier-induced stopping phase during the 2025 M_w 7.8 Myanmar earthquake: Evidence from near-fault strong motion observation. *Geophysical Research Letters*, *52*, e2025GL118863. https://doi.org/10.1029/2025GL118863

Received 21 AUG 2025
Accepted 22 NOV 2025

Author Contributions:

Conceptualization: Shiqing Xu, Lingling Ye
Formal analysis: Xiaotian Ding, Shiqing Xu, Lingling Ye
Funding acquisition: Shiqing Xu
Investigation: Xiaotian Ding
Project administration: Shiqing Xu
Software: Xiaotian Ding
Supervision: Shiqing Xu, Lingling Ye
Visualization: Xiaotian Ding, Lingling Ye
Writing – original draft: Xiaotian Ding, Shiqing Xu
Writing – review & editing: Xiaotian Ding, Shiqing Xu

Intermittent Supershear Rupture Punctuated by Barrier-Induced Stopping Phase During the 2025 M_w 7.8 Myanmar Earthquake: Evidence From Near-Fault Strong Motion Observation

Xiaotian Ding[1], Shiqing Xu[1], and Lingling Ye[1]

[1]Department of Earth and Space Sciences, Southern University of Science and Technology, Shenzhen, China

Abstract Supershear rupture has been investigated by many studies, yet its exact characteristics during natural earthquakes are not fully clear, due to the paucity of near-field constraints. Here we analyze the strong motion data recorded at a near-fault station during the 2025 M_w 7.8 Myanmar earthquake to estimate the detailed source process around that station. By comparing simulated velocity waveforms under various conditions with the observed one, we find that a supershear rupture with speed surpassing $\sqrt{2}$ times *S*-wave speed is required to fit the first-order features of the observation. Moreover, a fault barrier at ~6 km south of the station is inferred by the reversed-polarity fault-parallel secondary pulse following the main pulse, interpreted as a stopping phase. Together with other information, the results suggest an overall fast yet intermittent rupture process during the 2025 Myanmar earthquake, with the inferred barrier likely representing a segmentation boundary for the Sagaing fault.

Plain Language Summary There is an active debate on whether supershear rupture propagates continuously or intermittently, raising the need to investigate the detailed process of supershear rupture and the related wavefield characteristics. The 2025 M_w 7.8 Myanmar earthquake provides a good opportunity to probe this problem, due to the overall geometric simplicity of the central Sagaing fault that has long been proposed as a favorable condition for supershear rupture. In this study, we analyze the velocity waveform recorded at a near-fault station NPW to provide further insights into the source process of this earthquake. To do so, we conduct a series of computer simulations and compare the corresponding synthetic waveforms with the observed one. By optimizing waveform fit at the main pulse, we find that indeed a supershear rupture must be involved during the 2025 event. Moreover, a stopping phase indicative of fault barrier can be inferred by the reversed polarity of fault-parallel secondary velocity pulse. These results support a local intermittent source process with supershear rupture interrupted by a barrier, which is otherwise difficult to resolve by far-field observations. Our study suggests that more near-field observations should be deployed to enhance the resolution and understanding of earthquake source process.

1. Introduction

Characterizing earthquake sources is important for understanding earthquake physics and assessing seismic hazards. One key source parameter is the rupture speed. Considerable efforts have been made to clarify when rupture propagation can transition from below the *S*-wave speed (subshear) to above (supershear) (Andrews, 1976; Bao et al., 2022; D. Wang et al., 2016), partly because supershear rupture can generate damaging *S*-wave Mach front over a long off-fault distance (Bhat et al., 2007; Dunham & Archuleta, 2005). Subsequent studies (Cheng et al., 2023; Dunham, 2007) also suggest distinguishing between sustained supershear under relatively homogeneous conditions (Bouchon & Vallée, 2003; Bouchon et al., 2010; Liu et al., 2014; Robinson et al., 2010; Xia et al., 2004) and intermittent (or transient, episodic) supershear under heterogeneous conditions (Abdelmeguid et al., 2023; Bruhat et al., 2016; Delouis et al., 2024; Xu et al., 2023; Yao, 2017), thus it is important to test the related ideas using new observations.

Another important feature for studying earthquake sources is the reversed-polarity seismic phase produced by rupture arrest—called stopping phase (Page et al., 2005; Savage, 1965). Such phase is often accompanied by high-frequency radiation (especially under abrupt rupture arrest) (Madariaga, 1977, 1983), and it can be used to estimate source dimension and other parameters (Brüstle & Müller, 1987; Imanishi et al., 2004). Moreover, it is

thought to be able to produce small-scale, reversed-polarity volumetric deformation within a large-scale fault stepover, implying the potential of inferring earthquake directivity from geomorphological features (Ben-Zion et al., 2012). Despite these various applications, a stopping phase was rarely captured by in situ observations in the field, making it difficult to directly verify its related properties for natural earthquakes.

In this study, we show how supershear rupture and stopping phase can be jointly identified, based on the near-fault strong motion data recorded during the 2025 M_w 7.8 Myanmar earthquake. We further combine observed features with numerical simulations to infer a fault barrier within the overall rupture zone. The results demonstrate the high value of near-fault observations for constraining detailed source process.

2. The 2025 M_w 7.8 Myanmar Earthquake

This earthquake occurred on 28 March 2025, along the central section of the 1,400-km-long, right-lateral Sagaing fault that traverses Myanmar in the north-south direction (Figure 1a). Several significant earthquakes with magnitude above 6.5 had occurred along or near the Sagaing fault since 1839 (Y. Wang et al., 2014), but otherwise left a prominent seismic gap in the geometrically simple section in the center (Figure 1a), which has been anticipated to host a damaging, potentially supershear earthquake in the future (Hurukawa & Maung Maung, 2011; Robinson et al., 2010; Xiong et al., 2017). The 2025 M_w 7.8 event not only filled the identified seismic gap, but also penetrated into previously ruptured sections further to the north and south (Li et al., 2025; Ye et al., 2025).

Several research groups have estimated the source process of the 2025 event, revealing the following first-order picture (Inoue et al., 2025; Ye et al., 2025). The earthquake started near the city Mandalay, and then expanded energetically over ~50 km in both north and south directions. After about 40 s, it turned into a unilateral rupture primarily propagating to the south and continued for another 50 s. The final rupture had a total length of 460–480 km (Figure 1b), representing one of the longest strike-slip earthquakes, possibly aided by rupture along a bimaterial interface (Shi & Ben-Zion, 2006) and a narrowed rupture zone with gradually tapered slip toward the south (Li et al., 2025; USGS, 2025).

Regarding the details, while some studies imply a relatively smooth source process including a sustained supershear toward the south (Li et al., 2025; Vera et al., 2025), others suggest otherwise. For instance, the inverted results based on teleseismic data (e.g., Inoue et al., 2025; Ye et al., 2025) show a rather patchy slip distribution, with high slip concentrated around the hypocenter and ~180 km to the south (Figure 1b). Analyses of data recorded at a near-fault Closed Circuit Television (CCTV) camera and strong motion station NPW (see locations in Figure 1) also favor an intermittent source process with episodic rupture deceleration and acceleration (Hirano et al., 2025). Below we analyze the data recorded at the NPW station (near the city Nay Pyi Taw) to further support the view of intermittent source process, by highlighting a supershear rupture punctuated by barrier-induced stopping phase.

3. Data and Methods

3.1. Strong Motion Data at the NPW Station

The raw strong motion data recorded at the NPW station, corresponding to the unprocessed acceleration, were downloaded from the NSF Seismological Facility for the Advancement of Geoscience (SAGE) Data Management Center. We removed the instrument response and applied baseline correction using the method proposed by R. Wang et al. (2011). We did not make correction for the clock drift, since the accumulative time error was less than 1 s (Lai et al., 2025), which would not significantly affect the subsequent waveform analysis. Then we integrated the processed acceleration over time to obtain ground velocity, and rotated the results into fault-parallel (FP), fault-normal (FN), and up-down (UD) components based on the local fault geometry (Figures 1a and 1c), with positive indicating N7°W, N83°E and up, respectively.

For convenience, we divide the velocity waveform into four stages (Figure 1c): early part (Stage-I, 48.54–52.21 s), main pulse (Stage-II, 52.22–54.55 s), secondary pulse (Stage-III, 54.56–57.01 s), and trailing part (Stage-IV, 57.02–60.00 s). Starting with the main pulse (Stage-II), a simple comparison between the FP and FN components yields an amplitude ratio of $\Delta \dot{u}^s_{FP}/\Delta \dot{u}^s_{FN} = \sqrt{V_r^2/C_S^2 - 1} > 1$ ($\Delta \dot{u}^s_{FP}$ and $\Delta \dot{u}^s_{FN}$: zero-to-max amplitude of *S*-wave ground velocity in the FP and FN directions; V_r: rupture speed; and C_S: *S*-wave speed),

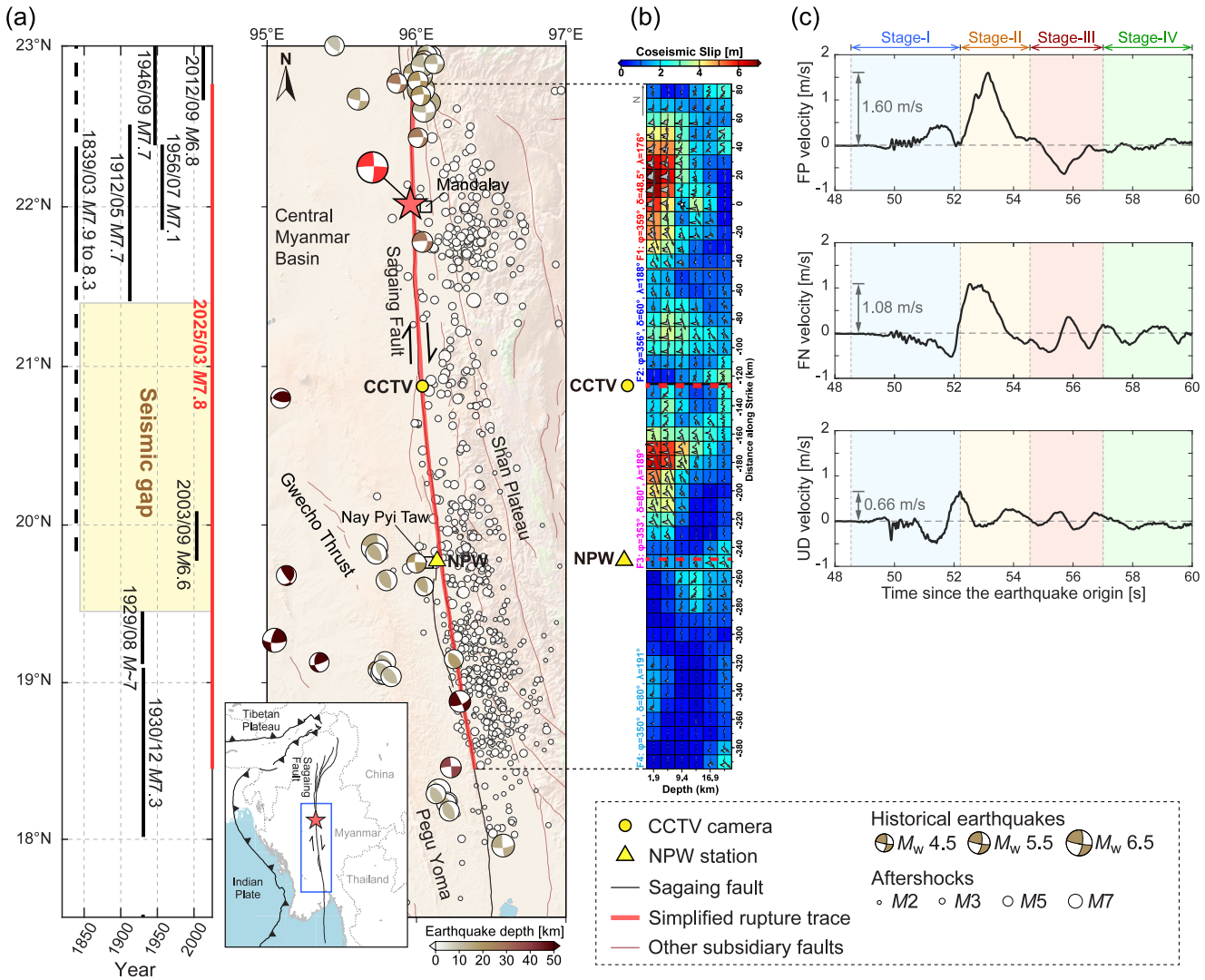

Figure 1. (a) Recent large earthquakes and tectonic setting for the studied area around the Sagaing fault in Myanmar. On the left, solid (dashed) black lines show the (inferred) extents of recent large earthquakes (Y. Wang et al., 2014), with a seismic gap (yellow box) in the center until the occurrence of the 2025 M_w 7.8 earthquake (solid red line). On the right, black and brown lines show the Sagaing fault and other subsidiary faults, respectively. The ruptured portion of the Sagaing fault during the 2025 earthquake is highlighted in red (modified after Benz et al. (2025)), with the red pentagram indicating the epicenter (Ye et al., 2025). Beachballs show the focal mechanisms for some historical earthquakes color-coded with source depth (01 January 1976–27 March 2025) and the 2025 mainshock (the red beachball, with M_w 7.7), based on the Global Centroid Moment Tensor catalog. Open circles show the aftershocks following the 2025 mainshock (28 March 2025–28 April 2025), based on the Thai Meteorological Department catalog. Yellow circle and triangle indicate the location of a Closed Circuit Television camera and strong motion station (NPW) near the Sagaing fault, respectively. (b) Coseismic source model over four subfaults (F1–F4) for the 2025 Myanmar earthquake, taken from Ye et al. (2025). Color shows the magnitude of slip on each subfault patch, with vectors indicating slip direction (eastern side relative to western side) and slip amount (implied by vector length), and gray polygons indicating the corresponding subfault source time function. (c) Three-component, velocity waveform recorded at the NPW station (see text for more details).

indicating a local rupture speed above $\sqrt{2}C_S$ (Mello et al., 2016). This estimation is consistent with the detailed waveform pattern at the FP main pulse (Stage-II), where the *S*-wave Mach front appears as a local peak (rather than a local trough) following the initial peak of the *P*-wave dilatational field (Figure 2d in Dunham and Archuleta (2005)). It is also interesting to note that the UD component generally shows an opposite polarity to the FP component during Stage-I, and the FP secondary pulse (Stage-III) shows an opposite polarity to the FP main pulse (Stage-II) (Figure 1c). While the former may reflect the Poisson effect related to head and direct waves (Section 5), the latter is less intuitive to understand and will be investigated by numerical simulations.

3.2. Setup of Numerical Simulations

To provide additional insights into the source process near the NPW station, we conduct numerical simulations of dynamic ruptures. The setup of numerical simulations is based on the kinematic source model of Ye et al. (2025), which shows a cascading rupture process over four subfaults (Figure 1b). Previous studies suggest that each episode in a cascading rupture process may be considered as a subevent, with renewed initial state taking into account the stress transfer from the earlier episode(s) (Ding et al., 2023; Xu et al., 2023). Therefore, here we do not model the 2025 Myanmar earthquake from the very beginning, but rather focus on the rupture process on subfault F3 (Figure 1b), with a particular interest in comparing simulated synthetic waveform with the observed one at the NPW station. This choice is justified by the smaller amplitude of waves radiated by the earlier-stage rupture (Figure 2f in Ye et al. (2025)), and the elongated earthquake rupture zone (Figure 1b) where pulse-like rupture can quickly prevail without strong dependence on rupture length (Text S1 in Supporting Information S1). Meanwhile, we also recognize some limitations of the above choice and will mention them in Section 5.

We simulate both 2.5D and 3D dynamic ruptures along a vertical, ~7.5 km-wide strike-slip subfault (after mapping to half space), following and simplifying the inverted results for F3 (Figure 1b). The 2.5D simulations are used to explore the waveform fit in both the FP and FN components over a large parameter space, while the 3D simulations are used to check the additional fit in the UD component. Time-weakening and slip-weakening friction laws are respectively employed to control the rupture evolution within and beyond the nucleation stage, as in Ding et al. (2023). We test a variety of rupture modes and speeds approaching the target NPW station, by tuning rupture nucleation and other conditions on the modeled subfault. Given the inverted result that the NPW station resides close to a local slip minimum (Figure 1b), we sometimes include a fault barrier in numerical simulations to investigate its impact on the synthetic waveform. For all cases, we assume rupture propagates along the main strand of the Sagaing fault, in accordance with the geodetic observations (Wei et al., 2025). We don't consider subsidiary faults (Figure 10 in Y. Wang et al. (2014)) in numerical simulations, despite their potential roles in affecting rupture path and wavefield characteristics. More details about numerical simulations are given in Text S1–S9, Figures S1–S5, and Tables S1 and S2 in Supporting Information S1.

4. Results

4.1. Reference Cases Without a Fault Barrier

We first examine the reference cases without a fault barrier. Figure 2 presents the simulated velocity field under the 2.5D model and the related waveform fit for two supershear ruptures with $V_r > \sqrt{2}C_S$ ($C_S = 3{,}310$ m/s, Text S2 in Supporting Information S1). As can be seen, both cases, though somewhat underestimating the FN main pulse, provide an overall good fit to the FP main pulse, including the general amplitude and the appearance of two local peaks (Stage-II in Figures 2b and 2d). Our additional tests show that a subshear rupture or an incipient supershear rupture that has just transitioned from subshear tends to produce a larger FN main pulse than the FP counterpart, inconsistent with the observation (Figures S6 and S7 in Supporting Information S1). Moreover, a (quasi)steady-state supershear rupture with $V_r \lesssim \sqrt{2}C_S$ tends to produce an *S*-wave trough behind the initial *P*-wave peak in the FP component or out-of-phase FP and FN main pulses, also inconsistent with the observation (Figure S8 in Supporting Information S1). Returning to Figure 2, the first case (Figures 2a and 2b), simulated under a mother-daughter transition (MDT), shows a stronger trailing Rayleigh phase than the second case (Figures 2c and 2d) under a direct transition (DT) (see Bizzarri and Liu (2016) and Xu et al. (2023) for more information about MDT and DT). In particular, the first case under MDT produces a much larger trailing pulse than the main pulse in the FN component, incompatible with the observed trend (Figure 2b). Based on all the above, we conclude that a well-developed supershear rupture, likely with $V_r > \sqrt{2}C_S$ but without strong trailing Rayleigh phase(s), is required to fit the first-order features of the observation at the NPW station. We also note that the supershear case under DT (Figure 2c), though satisfying the above requirement, still cannot fit the observed negative FP pulse during Stage-III (Figure 2d), which calls for the need to incorporate other model ingredients.

4.2. Preferred Cases With a Fault Barrier

Inspired by the known properties of stopping phase (Section 1) and the close proximity of NPW station to a local slip minimum (Section 3.2), we further incorporate a fault barrier into the supershear cases under DT, in order to test if the added barrier can cause a reversed-polarity secondary pulse in the FP component. Simulated results

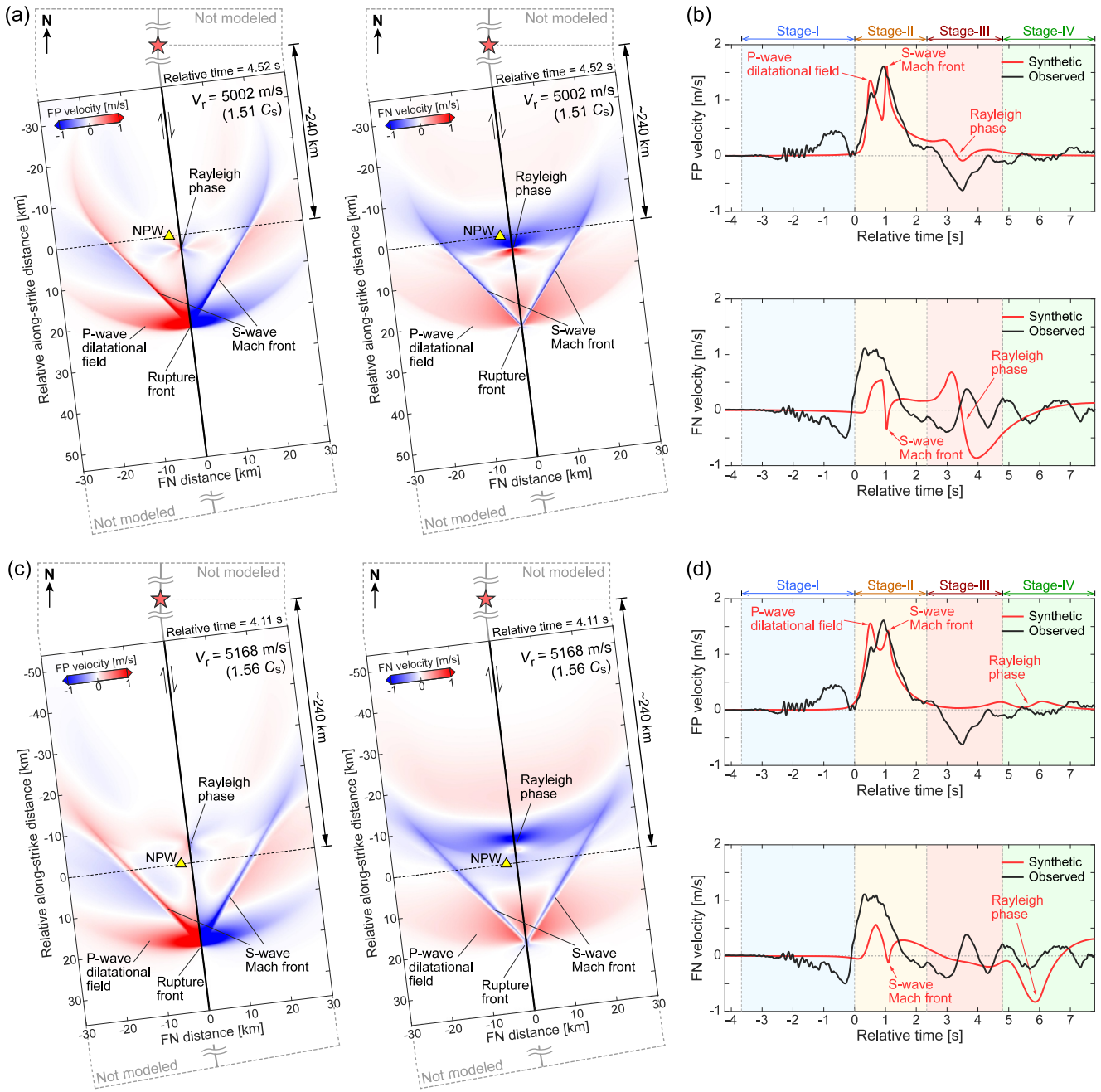

Figure 2. Wavefield characteristics for two reference cases under the 2.5D model. (a, b) The simulated velocity wavefield for a supershear rupture under a mother-daughter transition and the related waveform fit with data at the NPW station. (c, d) Similar results as in panels (a, b) but for a supershear rupture under a direct transition. In panels (a, c), relative along-strike distance zero is aligned to the NPW station, which itself is ~240 km south of the epicenter (red pentagram) and ~2.5 km west of the fault (Lai et al., 2025). In panels (b, d), relative time zero is aligned to the onset of observed fault-parallel pulse (in black) during Stage-II.

under the 2.5D model show that indeed the barrier, here modeled as a patch with spatially decreased initial shear stress, can produce a negative secondary velocity pulse (Stage-III) in the FP component (Figure 3b). By comparing more near-fault synthetic waveforms with the evolution of on-fault slip velocity, we find that the negative pulse observed at the NPW station is associated to the northward-propagating part of a stopping phase (Figure 3a and Figure S9 in Supporting Information S1). While such phase can cause a negative FP velocity off the fault, in the performed simulations it only permits a temporary relocking (zero instead of negative slip velocity) exactly on the fault due to frictional constraint (Figure S9 in Supporting Information S1). We further

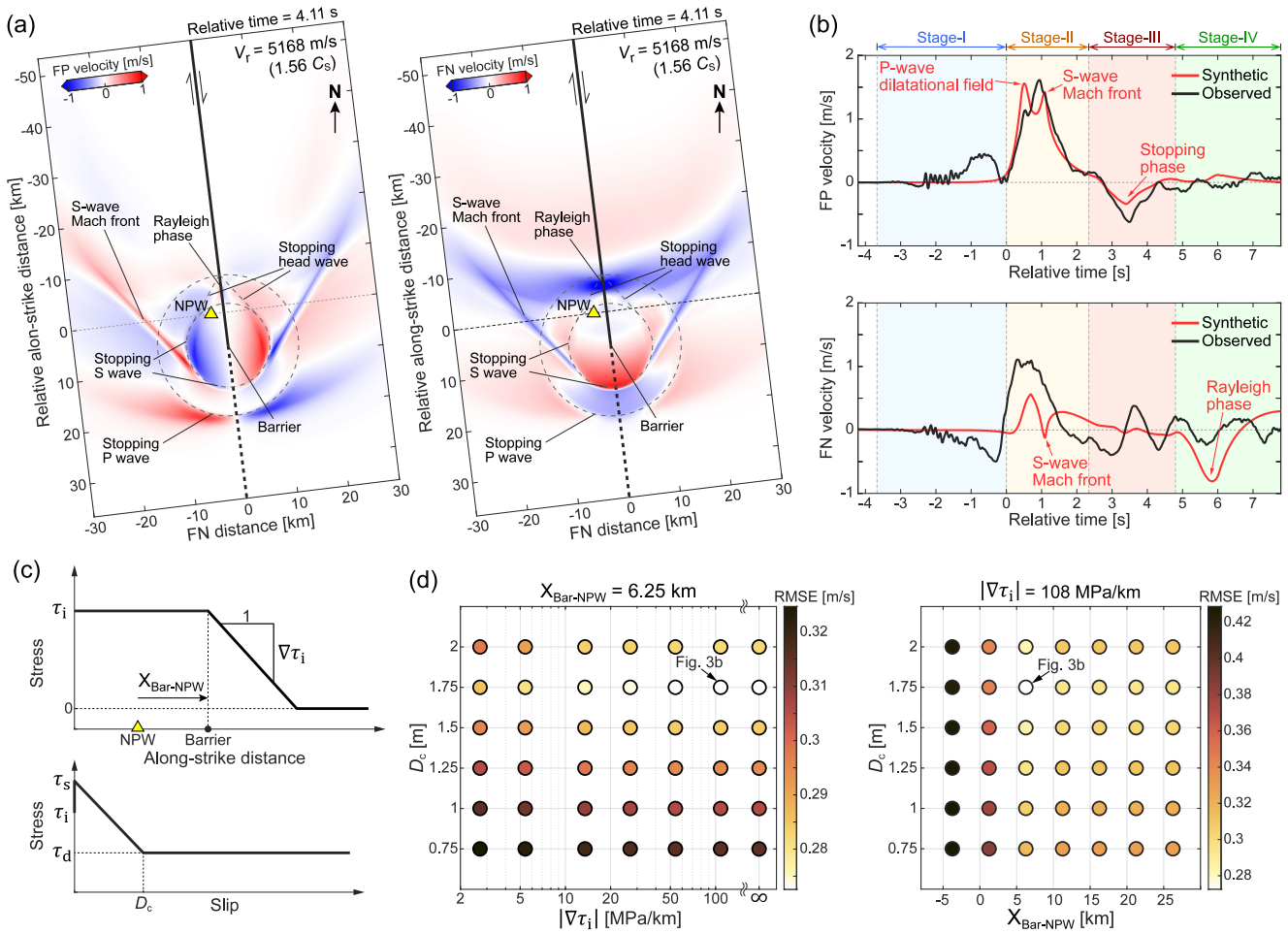

Figure 3. Wavefield characteristics for a preferred case under the 2.5D model and the related phase diagrams for constraining the properties of an added barrier. (a, b) The simulated velocity wavefield for a barrier-impeded supershear rupture under direct transition and the related waveform fit with data at the NPW station. In panel (a), major wavefronts of the stopping phase are marked by dashed lines. (c) Definitions of decreasing gradient of initial shear stress ($\nabla\tau_i$), location of barrier relative to NPW station ($X_{Bar\text{-}NPW}$) and slip-weakening distance (D_c), with τ_s and τ_d indicating static and dynamic strength, respectively (Text S3 in Supporting Information S1). (d) Phase diagrams summarizing waveform fit in terms of root-mean-square-error (see Text S8 in Supporting Information S1) over a range of D_c, $|\nabla\tau_i|$, and $X_{Bar\text{-}NPW}$.

conduct a detailed parameter-space study, by exploring waveform fit against data during Stage-I to III (Text S8 in Supporting Information S1) under various conditions of (negative) stress gradient, barrier location and slip-weakening distance (Figure 3c). The results suggest that in the preferred case(s) the barrier should be located at ~6 km south of the NPW station, and the absolute value of stress gradient must be relatively high (Figure 3d), otherwise the relative timing from the main pulse or the amplitude of the negative FP pulse cannot be reproduced (Figures S10–S12 in Supporting Information S1). We also make another set of tests by replacing decreased initial shear stress with increased normal stress or static friction coefficient, and obtain similar conclusions (Figures S13 and S14 in Supporting Information S1). By transforming the preferred case(s) from 2.5D to 3D under a comparable model setup (Text S1 in Supporting Information S1), we find that the transformed case(s) can also provide a good fit to the UD component, at least during Stage-II and/or III (Figures S15–S17 in Supporting Information S1).

5. Discussion and Conclusions

We have analyzed the near-fault strong motion data recorded at the NPW station for the 2025 M_w 7.8 Myanmar earthquake. By integrating the observed waveform characteristics, simulation results and other available information, we now provide an in-depth discussion on the source process of this earthquake. At the macroscopic

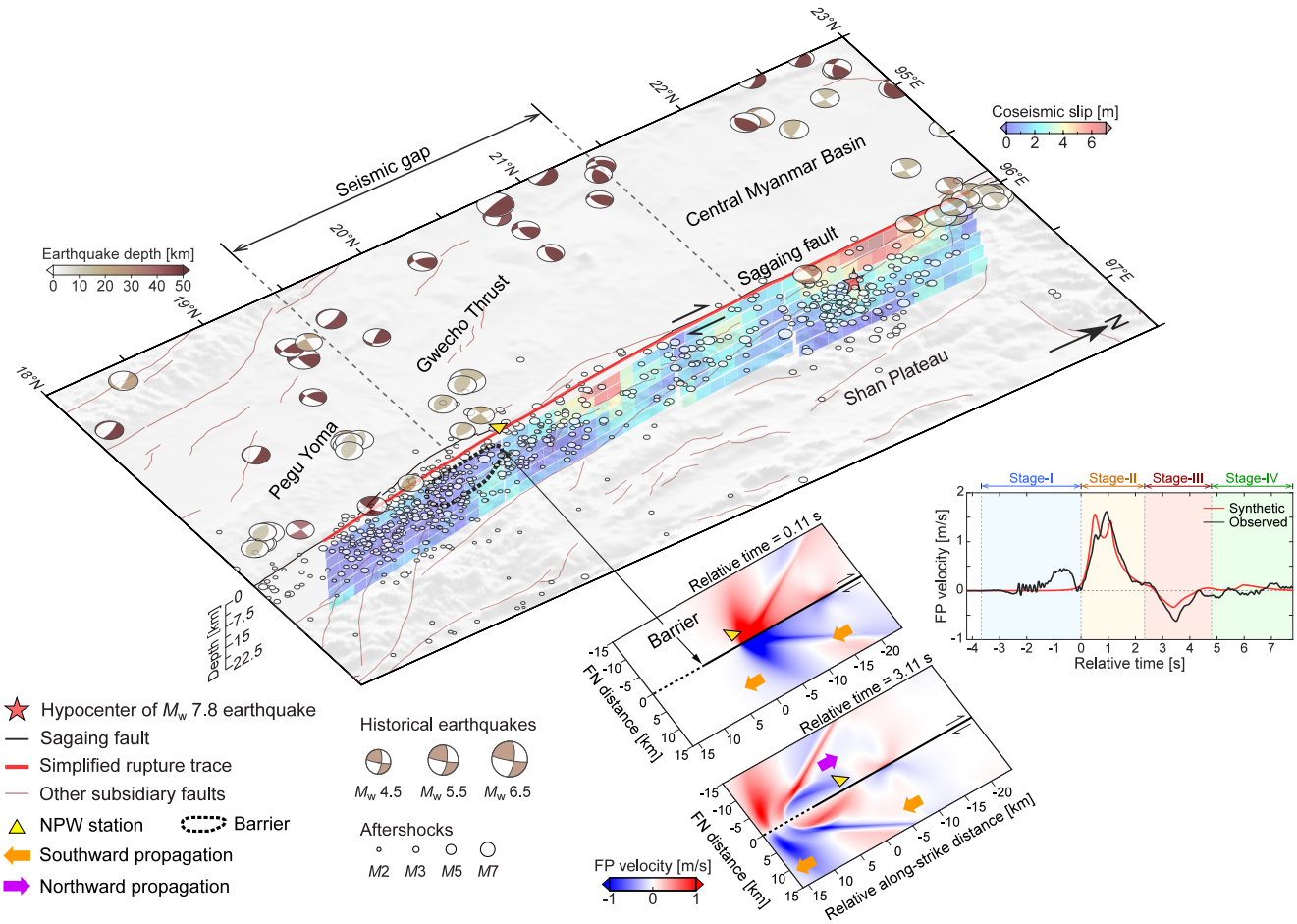

Figure 4. Perspective view of seismological and geological features around the 2025 M_w 7.8 Myanmar earthquake rupture zone. Color-coded beachballs show the focal mechanisms and depth information for some historical earthquakes according to the Global Centroid Moment Tensor catalog, and open circles show the distribution of aftershocks (projected onto ground surface) according to the Thai Meteorological Department catalog (see Figure 1 for more information). Color-coded patches show the coseismic slip distribution determined by Ye et al. (2025), with the red pentagram indicating the mainshock hypocenter. Plots at the bottom right show the simulated fault-parallel velocity under the preferred case and the corresponding waveform fit with data. The position and possible spatial extent of the inferred barrier are depicted by the dashed black line to the south of the NPW station.

scale, the southward rupture did not propagate smoothly with an average supershear speed of 4,615 m/s ($\lesssim\sqrt{2}C_S$) (according to the epicentral distance of ~240 km and the arrival time of ~52 s at the NPW station), but had episodic deceleration and acceleration, possibly involving supershear around the hypocenter, subshear around the CCTV camera and supershear again (likely with $V_r > \sqrt{2}C_S$) around the NPW station (Hirano et al., 2025; Inoue et al., 2025; Figures 1 and 3). This large-scale intermittent process is also supported by the coseismic slip distribution, with one low slip patch lying between two high ones (Inoue et al., 2025; Ye et al., 2025; Figure 4), corresponding to the estimated subshear and supershear episode(s), respectively (Hirano et al., 2025). Similar rupture behaviors, characterized by supershear-subshear-supershear transition and undulant slip distribution, have been repeatedly observed on a laboratory fault with stress heterogeneities (Xu et al., 2023), suggesting that the 2025 Myanmar earthquake may also be modulated by stress heterogeneities.

At the local scale, the rupture evolution on subfault F3 showed multiple slip pulses associated with strong spatial heterogeneity (Figure 1b) and was impacted by an inferred barrier near the NPW station (Figures 3 and 4), also contributing to an intermittent process. More evidences for the inferred barrier can involve the following features near the NPW station: (a) high-frequency source radiators (Li et al., 2025) including some back-propagating ones (Vera et al., 2025), (b) clustered aftershocks in contrast with fewer ones to the north (Peng et al., 2025; Figure 4), (c) coincidence with the southern end of the previously identified seismic gap (Li et al., 2025; Figure 4), (d) relatively low slip and/or low stress drop reported by other studies (Li et al., 2025; USGS, 2025), (e) structural

complexities such as fault discontinuity, branching, and bend (Figure 19.9c in Tun and Watkinson (2017); Figure 4), and (f) localized reverse-type faulting and seismicity (Figure 19.2 in Tun and Watkinson (2017); Figure 4) indicating a local high angle of maximum compressive stress to the Sagaing fault (see Mount and Suppe (1987) and Miller (1998) for a corresponding discussion on the San Andreas fault). Therefore, although we cannot rule out other possibilities for interpreting the negative FP secondary velocity pulse recorded at the NPW station, such as the negative loading from fault-zone-reflected waves (Huang & Ampuero, 2011), we think barrier-induced stopping phase should stand out as a strongly supported explanation (Figures 3 and 4, Figures S15–S17 in Supporting Information S1). While we have further constrained the starting position and strength of the inferred barrier (Figure 3, Figures S13 and S14 in Supporting Information S1), it is difficult to estimate its ending position on the other side by current simulations. Nonetheless, we expect the barrier to exhibit a moderate size at most (Figure 4), since the actual rupture could continue its propagation further to the south (USGS, 2025; Ye et al., 2025).

Taken together, the discussed intermittent source process supports the view of fault segmentation as one of the criteria for distinguishing some large earthquakes from small ones (Aki, 1984; Cui et al., 2025; Klinger, 2022; Lay & Kanamori, 1981; Manighetti et al., 2007; Xu et al., 2018). Specifically, the inferred barrier near the NPW station (Figure 4) likely represents a segmentation boundary for the Sagaing fault. On one hand, it may serve as an external barrier to fully stop some small earthquakes around 19.5°N (Figure 1), with their sources described by a compact, simply connected region (Manighetti et al., 2007) with near-constant rupture speed (Kaneko & Shearer, 2015). Under such condition, observable high-frequency radiation to the far field mainly reflects the starting and/or stopping of the overall rupture process (Li et al., 2022; Madariaga, 1977). On the other hand, it can behave as an internal barrier (e.g., partially ruptured or bypassed patch) within the overall source region of an elongated large earthquake, with ability to cause additional high-frequency radiation, internal stress drop deficit or even stress concentration, and multiple peaks in moment rate function (Madariaga, 1979), as supported by the observational results for the 2025 M_w 7.8 event (Li et al., 2025; Vera et al., 2025; Ye et al., 2025).

It is worth noting that some of the observed waveform features still cannot be fitted by the preferred synthetics (Figure 3), including (a) earlier signals carrying some high-frequency content during Stage-I, (b) the descending slope without a subsequent ascending one at the FN main pulse during Stage-II, and (c) the enduring oscillations during Stage-III and IV. This suggests that more complexities may be involved in the 2025 Myanmar earthquake but are not modeled by current simulations. Nonetheless, we can propose tentative ideas for understanding these features, assuming that they reflect true source, path or site effects rather than instrumental errors. Due to the earlier arrival, feature-(a) may represent head wave refracted from the Moho or the bimaterial Sagaing fault (Ben-Zion, 1990) and/or direct wave radiated by earlier-stage rupture (Peng et al., 2025), with the high-frequency content indicating *P*-wave-triggered failure or nonlinear response in the shallow subsurface (Sleep, 2018; Sleep & Ma, 2008) and/or local damage-related radiation (Ben-Zion et al., 2024). Feature-(b) is rather intriguing at first glance, as it would contrast with the predicted opposite polarities for FP and FN components at the Mach front (Figure 2 and Figure S8 in Supporting Information S1), where pure shear deformation (zero divergence) is expected to dominate (Mello et al., 2016). Possible ways for reconciling this conflict and the mismatch in FN pulse amplitude could be to incorporate a depth-varying source process (Figure 1b), material heterogeneity (Abdelmeguid et al., 2025; Xu & Ben-Zion, 2017), or structural complexity such as fault branches (Y. Wang et al., 2014). Finally, feature-(c) may stem from various trapping effects of a sedimentary basin (Somerville & Graves, 2003) or low-velocity fault zone (Huang & Ampuero, 2011; Xu et al., 2015). Future work can be done to test the above ideas via more sophisticated 3D numerical simulations.

In summary, our study by identifying supershear rupture and stopping phase at a near-fault strong motion station has provided valuable insights into the 2025 M_w 7.8 Myanmar earthquake, such as an intermittent source process and the existence of a fault barrier. The results once again demonstrate the high value of near-fault observations (Ben-Zion, 2019). With more deployments of near-fault observations, more properties previously proposed for earthquake sources can be tested, while some unexpected, new results may be discovered as well.

Conflict of Interest

The authors declare no conflicts of interest relevant to this study.

Data Availability Statement

The software SEM2DPACK for conducting 2.5D simulations is available at https://github.com/jpampuero/sem2dpack (Ampuero, 2012). The software SPECFEM3D for conducting 3D simulations is available at https://doi.org/10.5281/zenodo.10823181 (Komatitsch et al., 2024). The input parameters for performing numerical simulations are within the paper. The database for geological faults in Myanmar is available at https://doi.org/10.13140/RG.2.2.25509.58084 (Bachmanov et al., 2022). The surface rupture trace data for the 2025 Myanmar earthquake can be found from Benz et al. (2025). Information of earthquake focal mechanisms can be found from the Global Centroid Moment Tensor (GCMT) project (Ekström et al., 2012). Information of aftershocks can be found at https://www.fdsn.org/networks/detail/TM/ (Thai Meteorological Department, 2008). The raw strong motion data can be downloaded from the NSF Seismological Facility for the Advancement of Geoscience (SAGE) (https://ds.iris.edu/wilber3/find_stations/11952284). Some of the figures were drawn by the Generic Mapping Tools (GMT) (Wessel et al., 2019).

Acknowledgments
This study was supported by the National Natural Science Foundation of China (42474082) and the Guangdong Program (2021QN02G106).

References

Abdelmeguid, M., Elbanna, A., & Rosakis, A. (2025). Ground motion characteristics of subshear and supershear ruptures in the presence of sediment layers. *Geophysical Journal International*, *240*(2), 967–987. https://doi.org/10.1093/gji/ggae422

Abdelmeguid, M., Zhao, C., Yalcinkaya, E., Gazetas, G., Elbanna, A., & Rosakis, A. (2023). Dynamics of episodic supershear in the 2023 M7.8 Kahramanmaraş/Pazarcik earthquake, revealed by near-field records and computational modeling. *Communications Earth & Environment*, *4*(1), 456. https://doi.org/10.1038/s43247-023-01131-7

Aki, K. (1984). Asperities, barriers, characteristic earthquakes and strong motion prediction. *Journal of Geophysical Research*, *89*(B7), 5867–5872. https://doi.org/10.1029/JB089iB07p05867

Ampuero, J.-P. (2012). SEM2DPACK—A spectral element method tool for 2D wave propagation and earthquake source dynamics [Software]. Retrieved from https://github.com/jpampuero/sem2dpack

Andrews, D. J. (1976). Rupture velocity of plane strain shear cracks. *Journal of Geophysical Research*, *81*(32), 5679–5687. https://doi.org/10.1029/JB081i032p05679

Bachmanov, D. M., Trifonov, V. G., Kozhurin, A. I., & Zelenin, E. A. (2022). Active faults of Eurasia database AFEAD v2022 [Dataset]. *ResearchGate*. https://doi.org/10.13140/RG.2.2.25509.58084

Bao, H., Xu, L., Meng, L., Ampuero, J.-P., Gao, L., & Zhang, H. (2022). Global frequency of oceanic and continental supershear earthquakes. *Nature Geoscience*, *15*(11), 942–949. https://doi.org/10.1038/s41561-022-01055-5

Benz, H., Furlong, K., Herman, M., McKenzie, K., Schmitt, R., Reitman, N., et al. (2025). 2025 M 7.7 Mandalay, Burma (Myanmar) earthquake [Dataset]. *U.S. Geological Survey StoryMap*. Retrieved from https://storymaps.arcgis.com/stories/5f3e33e35c5247c9bf5204fa0d6e56e5

Ben-Zion, Y. (1990). The response of two half spaces to point dislocations at the material interface. *Geophysical Journal International*, *101*(3), 507–528. https://doi.org/10.1111/j.1365-246X.1990.tb05567.x

Ben-Zion, Y. (2019). A critical data gap in earthquake physics. *Seismological Research Letters*, *90*(5), 1721–1722. https://doi.org/10.1785/0220190167

Ben-Zion, Y., Rockwell, T. K., Shi, Z., & Xu, S. (2012). Reversed-polarity secondary deformation structures near fault stepovers. *Journal of Applied Mechanics*, *79*(3), 031025. https://doi.org/10.1115/1.4006154

Ben-Zion, Y., Zhang, S., & Meng, X. (2024). Isotropic high-frequency radiation in near-fault seismic data. *Geophysical Research Letters*, *51*(17), e2024GL110303. https://doi.org/10.1029/2024GL110303

Bhat, H. S., Dmowska, R., King, G. C. P., Klinger, Y., & Rice, J. R. (2007). Off-fault damage patterns due to supershear ruptures with application to the 2001 M_w 8.1 Kokoxili (Kunlun) Tibet earthquake. *Journal of Geophysical Research*, *112*(B6), B06301. https://doi.org/10.1029/2006JB004425

Bizzarri, A., & Liu, C. (2016). Near-field radiated wave field may help to understand the style of the supershear transition of dynamic ruptures. *Physics of the Earth and Planetary Interiors*, *261*, 133–140. https://doi.org/10.1016/j.pepi.2016.05.013

Bouchon, M., Karabulut, H., Bouin, M.-P., Schmittbuhl, J., Vallée, M., Archuleta, R., et al. (2010). Faulting characteristics of supershear earthquakes. *Tectonophysics*, *493*(3–4), 244–253. https://doi.org/10.1016/j.tecto.2010.06.011

Bouchon, M., & Vallée, M. (2003). Observation of long supershear rupture during the magnitude 8.1 Kunlunshan earthquake. *Science*, *301*(5634), 824–826. https://doi.org/10.1126/science.1086832

Bruhat, L., Fang, Z., & Dunham, E. M. (2016). Rupture complexity and the supershear transition on rough faults. *Journal of Geophysical Research: Solid Earth*, *121*(1), 210–224. https://doi.org/10.1002/2015JB012512

Brüstle, W., & Müller, G. (1987). Stopping phases in seismograms and the spatiotemporal extent of earthquakes. *Bulletin of the Seismological Society of America*, *77*(1), 47–68. https://doi.org/10.1785/BSSA0770010047

Cheng, C., Wang, D., Yao, Q., Fang, L., Xu, S., Huang, Z., et al. (2023). The 2021 Mw 7.3 Madoi, China earthquake: Transient supershear ruptures on a presumed immature strike-slip fault. *Journal of Geophysical Research: Solid Earth*, *128*(2), e2022JB024641. https://doi.org/10.1029/2022JB024641

Cui, Y., Li, S., Chen, L., & Aoki, Y. (2025). Large megathrust earthquakes tend to sustain an increasingly longer duration than expected. *Geophysical Research Letters*, *52*(8), e2024GL112985. https://doi.org/10.1029/2024GL112985

Delouis, B., van den Ende, M., & Ampuero, J.-P. (2024). Kinematic rupture model of the 6 February 2023 M_w 7.8 Türkiye earthquake from a large set of near-source strong-motion records combined with GNSS offsets reveals intermittent supershear rupture. *Bulletin of the Seismological Society of America*, *114*(2), 726–740. https://doi.org/10.1785/0120230077

Ding, X., Xu, S., Xie, Y., van den Ende, M., Premus, J., & Ampuero, J.-P. (2023). The sharp turn: Backward rupture branching during the 2023 M_w 7.8 Kahramanmaraş (Türkiye) earthquake. *Seismica*, *2*(3). https://doi.org/10.26443/seismica.v2i3.1083

Dunham, E. M. (2007). Conditions governing the occurrence of supershear ruptures under slip-weakening friction. *Journal of Geophysical Research*, *112*(B7), B07302. https://doi.org/10.1029/2006JB004717

Dunham, E. M., & Archuleta, R. J. (2005). Near-source ground motion from steady state dynamic rupture pulses. *Geophysical Research Letters*, *32*(3), L03302. https://doi.org/10.1029/2004GL021793

Ekström, G., Nettles, M., & Dziewoński, A. M. (2012). The global CMT project 2004–2010: Centroid-moment tensors for 13,017 earthquakes. *Physics of the Earth and Planetary Interiors*, *200*, 1–9. https://doi.org/10.1016/j.pepi.2012.04.002

Hirano, S., Doke, R., & Maeda, T. (2025). Supershear-subshear-supershear rupture associated with the 2025 Mandalay earthquake in Myanmar. *Seismica*, *4*(2). https://doi.org/10.26443/seismica.v4i2.1785

Huang, Y., & Ampuero, J.-P. (2011). Pulse-like ruptures induced by low-velocity fault zones. *Journal of Geophysical Research*, *116*(B12), B12307. https://doi.org/10.1029/2011JB008684

Hurukawa, N., & Maung Maung, P. (2011). Two seismic gaps on the Sagaing fault, Myanmar, derived from relocation of historical earthquakes since 1918. *Geophysical Research Letters*, *38*(1), L01310. https://doi.org/10.1029/2010GL046099

Imanishi, K., Takeo, M., Ellsworth, W. L., Ito, H., Matsuzawa, T., Kuwahara, Y., et al. (2004). Source parameters and rupture velocities of microearthquakes in Western Nagano, Japan, determined using stopping phases. *Bulletin of the Seismological Society of America*, *94*(5), 1762–1780. https://doi.org/10.1785/012003085

Inoue, N., Yamaguchi, R., Yagi, Y., Okuwaki, R., Enescu, B., & Tadapansawut, T. (2025). A multiple asymmetric bilateral rupture sequence derived from the peculiar tele-seismic *P*-waves of the 2025 Mandalay, Myanmar earthquake. *Seismica*, *4*(1). https://doi.org/10.26443/seismica.v4i1.1691

Kaneko, Y., & Shearer, P. M. (2015). Variability of seismic source spectra, estimated stress drop, and radiated energy, derived from cohesive-zone models of symmetrical and asymmetrical circular and elliptical ruptures. *Journal of Geophysical Research: Solid Earth*, *120*(2), 1053–1079. https://doi.org/10.1002/2014JB011642

Klinger, Y. (2022). Imprint of the continental strike-slip fault geometrical structure in geophysical data. *Geophysical Research Letters*, *49*(11), e2022GL098146. https://doi.org/10.1029/2022GL098146

Komatitsch, D., Tromp, J., Garg, R., Gharti, H. N., Nagaso, M., Oral, E., et al. (2024). SPECFEM/specfem3d: SPECFEM3D v4.1.1 [Software]. *Zenodo*. https://doi.org/10.5281/zenodo.10823181

Lai, S.-T., Oo, K. M., Htwe, Y. M. M., Yi, T., Than, H. H., Than, O., et al. (2025). Capacity building enables unique near-fault observations of the destructive 2025 M_w 7.7 Myanmar earthquake. *Earth System Science Data Discussions*. https://doi.org/10.5194/essd-2025-216

Lay, T., & Kanamori, H. (1981). An asperity model of large earthquake sequences. In D. W. Simpson & P. G. Richards (Eds.), *Earthquake prediction: An international review, maurice ewing series* (Vol. 4, pp. 579–592). American Geophysical Union. https://doi.org/10.1029/ME004p0579

Li, B., Jónsson, S., Suhendi, C., Liu, J., Li, D., Delorme, A., et al. (2025). Seismic gap breached by the 2025 M_w 7.7 Mandalay (Myanmar) earthquake. *Nature Geoscience*, 1–9. https://doi.org/10.1038/s41561-025-01861-7

Li, B., Wu, B., Bao, H., Oglesby, D. D., Ghosh, A., Gabriel, A.-A., et al. (2022). Rupture heterogeneity and directivity effects in back-projection analysis. *Journal of Geophysical Research: Solid Earth*, *127*(3), e2021JB022663. https://doi.org/10.1029/2021JB022663

Liu, C., Bizzarri, A., & Das, S. (2014). Progression of spontaneous in-plane shear faults from sub-Rayleigh to compressional wave rupture speeds. *Journal of Geophysical Research: Solid Earth*, *119*(11), 8331–8345. https://doi.org/10.1002/2014JB011187

Madariaga, R. (1977). High-frequency radiation from crack (stress drop) models of earthquake faulting. *Geophysical Journal International*, *51*(3), 625–651. https://doi.org/10.1111/j.1365-246X.1977.tb04211.x

Madariaga, R. (1979). On the relation between seismic moment and stress drop in the presence of stress and strength heterogeneity. *Journal of Geophysical Research*, *84*(B5), 2243–2250. https://doi.org/10.1029/JB084iB05p02243

Madariaga, R. (1983). High frequency radiation from dynamic earthquake fault models. *Annales de Geophysique*, *1*(1), 17–23.

Manighetti, I., Campillo, M., Bouley, S., & Cotton, F. (2007). Earthquake scaling, fault segmentation, and structural maturity. *Earth and Planetary Science Letters*, *253*(3–4), 429–438. https://doi.org/10.1016/j.epsl.2006.11.004

Mello, M., Bhat, H. S., & Rosakis, A. J. (2016). Spatiotemporal properties of sub-Rayleigh and supershear rupture velocity fields: Theory and experiments. *Journal of the Mechanics and Physics of Solids*, *93*, 153–181. https://doi.org/10.1016/j.jmps.2016.02.031

Miller, D. D. (1998). Distributed shear, rotation, and partitioned strain along the San Andreas fault, central California. *Geology*, *26*(10), 867–870. https://doi.org/10.1130/0091-7613(1998)026<0867:DSRAPS>2.3.CO;2

Mount, V. S., & Suppe, J. (1987). State of stress near the San Andreas fault: Implications for wrench tectonics. *Geology*, *15*(12), 1143–1146. https://doi.org/10.1130/0091-7613(1987)15<1143:SOSNTS>2.0.CO;2

Page, M. T., Dunham, E. M., & Carlson, J. M. (2005). Distinguishing barriers and asperities in near-source ground motion. *Journal of Geophysical Research*, *110*(B11), B11302. https://doi.org/10.1029/2005JB003736

Peng, Z., Lei, X., Wang, D., Si, X., Mach, P., Zhong, Q., et al. (2025). Mainshock rupture properties, aftershock activities and remotely triggered seismicity associated with the 2025 Mw7.7 Sagaing fault earthquake in Myanmar. *Earthquake Research Advances*, *5*(4), 100413. https://doi.org/10.1016/j.eqrea.2025.100413

Robinson, D. P., Das, S., & Searle, M. P. (2010). Earthquake fault superhighways. *Tectonophysics*, *493*(3–4), 236–243. https://doi.org/10.1016/j.tecto.2010.01.010

Savage, J. C. (1965). The stopping phase on seismograms. *Bulletin of the Seismological Society of America*, *55*(1), 47–58. https://doi.org/10.1785/BSSA0550010047

Shi, Z., & Ben-Zion, Y. (2006). Dynamic rupture on a bimaterial interface governed by slip-weakening friction. *Geophysical Journal International*, *165*(2), 469–484. https://doi.org/10.1111/j.1365-246X.2006.02853.x

Sleep, N. H. (2018). Searching for spot-fire earthquakes triggered during the 2004 Parkfield mainshock. In *Poster presentation at 2018 SCEC annual meeting*.

Sleep, N. H., & Ma, S. (2008). Production of brief extreme ground acceleration pulses by nonlinear mechanisms in the shallow subsurface. *Geochemistry, Geophysics, Geosystems*, *9*(3), Q03008. https://doi.org/10.1029/2007GC001863

Somerville, P. G., & Graves, R. W. (2003). Characterization of earthquake strong ground motion. *Pure and Applied Geophysics*, *160*(10–11), 1811–1828. https://doi.org/10.1007/s00024-003-2407-z

Thai Meteorological Department. (2008). *Thai seismic monitoring network*. International Federation of Digital Seismograph Networks. Retrieved from https://www.fdsn.org/networks/detail/TM/

Tun, S. T., & Watkinson, I. M. (2017). Chapter 19: The Sagaing fault, Myanmar. In A. J. Barber, K. Zaw, & M. J. Crow (Eds.), *Myanmar: Geology, resources and tectonics* (Vol. 48, pp. 413–441). London Geological Society. https://doi.org/10.1144/M48.19

USGS. (2025). Retrieved from https://earthquake.usgs.gov/earthquakes/eventpage/us7000pn9s/executive

Vera, F., Carrillo-Ponce, A., Crosetto, S., Kosari, E., Metzger, S., Motagh, M., et al. (2025). Supershear rupture along the Sagaing fault seismic gap: The 2025 Myanmar earthquake. *The Seismic Record*, *5*(3), 289–299. https://doi.org/10.1785/0320250025

Wang, D., Mori, J., & Koketsu, K. (2016). Fast rupture propagation for large strike-slip earthquakes. *Earth and Planetary Science Letters*, *440*, 115–126. https://doi.org/10.1016/j.epsl.2016.02.022

Wang, R., Schurr, B., Milkereit, C., Shao, Z., & Jin, M. (2011). An improved automatic scheme for empirical baseline correction of digital strong-motion records. *Bulletin of the Seismological Society of America*, *101*(5), 2029–2044. https://doi.org/10.1785/0120110039

Wang, Y., Sieh, K., Tun, S. T., Lai, K.-Y., & Myint, T. (2014). Active tectonics and earthquake potential of the Myanmar region. *Journal of Geophysical Research: Solid Earth*, *119*(4), 3767–3822. https://doi.org/10.1002/2013JB010762

Wei, S., Wang, X., Li, C., Zeng, H., Ma, Z., Shi, Q., et al. (2025). Supershear rupture sustained through a thick fault zone in the 2025 M_w 7.8 Mandalay earthquake. *Science*, *390*(6772), 468–475. https://doi.org/10.1126/science.adz2101

Wessel, P., Luis, J. F., Uieda, L., Scharroo, R., Wobbe, F., Smith, W. H. F., & Tian, D. (2019). The generic mapping tools version 6. *Geochemistry, Geophysics, Geosystems*, *20*(11), 5556–5564. https://doi.org/10.1029/2019GC008515

Xia, K., Rosakis, A. J., & Kanamori, H. (2004). Laboratory earthquakes: The sub-Rayleigh-to-supershear rupture transition. *Science*, *303*(5665), 1859–1861. https://doi.org/10.1126/science.1094022

Xiong, X., Shan, B., Zhou, Y. M., Wei, S. J., Li, Y. D., Wang, R. J., & Zheng, Y. (2017). Coulomb stress transfer and accumulation on the Sagaing fault, Myanmar, over the past 110 years and its implications for seismic hazard. *Geophysical Research Letters*, *44*(10), 4781–4789. https://doi.org/10.1002/2017GL072770

Xu, S., & Ben-Zion, Y. (2017). Theoretical constraints on dynamic pulverization of fault zone rocks. *Geophysical Journal International*, *209*(1), 282–296. https://doi.org/10.1093/gji/ggx033

Xu, S., Ben-Zion, Y., Ampuero, J.-P., & Lyakhovsky, V. (2015). Dynamic ruptures on a frictional interface with off-fault brittle damage: Feedback mechanisms and effects on slip and near-fault motion. *Pure and Applied Geophysics*, *172*(5), 1243–1267. https://doi.org/10.1007/s00024-014-0923-7

Xu, S., Fukuyama, E., Yamashita, F., Kawakata, H., Mizoguchi, K., & Takizawa, S. (2023). Fault strength and rupture process controlled by fault surface topography. *Nature Geoscience*, *16*(1), 94–100. https://doi.org/10.1038/s41561-022-01093-z

Xu, S., Fukuyama, E., Yamashita, F., Mizoguchi, K., Takizawa, S., & Kawakata, H. (2018). Strain rate effect on fault slip and rupture evolution: Insight from meter-scale rock friction experiments. *Tectonophysics*, *733*, 209–231. https://doi.org/10.1016/j.tecto.2017.11.039

Yao, Q. (2017). *Dynamic modeling of earthquake sources on rough faults*. (Doctoral dissertation). University of California, San Diego & San Diego State University.

Ye, L., Lay, T., & Kanamori, H. (2025). The 28 March 2025 M_w 7.8 Myanmar earthquake: Preliminary analysis of an ~480 km long intermittent supershear rupture. *The Seismic Record*, *5*(3), 260–269. https://doi.org/10.1785/0320250021

References From the Supporting Information

Aki, K., & Richards, P. G. (2002). *Quantitative seismology* (2nd ed.). University Science Books.

Brocher, T. M. (2005). Empirical relations between elastic wavespeeds and density in the Earth's crust. *Bulletin of the Seismological Society of America*, *95*(6), 2081–2092. https://doi.org/10.1785/0120050077

Day, S. (1982). Three-dimensional finite difference simulation of fault dynamics: Rectangular faults with fixed rupture velocity. *Bulletin of the Seismological Society of America*, *72*(3), 705–727. https://doi.org/10.1785/BSSA0720030705

Dunham, E. M., & Archuleta, R. J. (2004). Evidence for a supershear transient during the 2002 Denali fault earthquake. *Bulletin of the Seismological Society of America*, *94*(6B), S256–S268. https://doi.org/10.1785/0120040616

Kaneko, Y., & Lapusta, N. (2010). Supershear transition due to a free surface in 3-D simulations of spontaneous dynamic rupture on vertical strike-slip faults. *Tectonophysics*, *493*(3–4), 272–284. https://doi.org/10.1016/j.tecto.2010.06.015

Luo, Y., Ampuero, J.-P., Miyakoshi, K., & Irikura, K. (2017). Surface rupture effects on earthquake moment-area scaling relations. *Pure and Applied Geophysics*, *174*(9), 3331–3342. https://doi.org/10.1007/s00024-017-1467-4

Ma, S. (2008). A physical model for widespread near-surface and fault zone damage induced by earthquakes. *Geochemistry, Geophysics, Geosystems*, *9*(11), Q11009. https://doi.org/10.1029/2008GC002231

Pollard, D. D., & Segall, P. (1987). Theoretical displacements and stresses near fractures in rock: With applications to faults, joints, veins, dikes, and solution surfaces. In B. K. Atkinson (Ed.), *Fracture mechanics of rock* (Vol. 8, pp. 277–349). London Academic Press. https://doi.org/10.1016/b978-0-12-066266-1.50013-2

Shiddiqi, H. A., Tun, P. P., & Ottemöller, L. (2019). Minimum 1D velocity model and local magnitude scale for Myanmar. *Seismological Research Letters*, *90*(5), 1923–1936. https://doi.org/10.1785/0220190065

Weng, H., & Ampuero, J.-P. (2019). The dynamics of elongated earthquake ruptures. *Journal of Geophysical Research: Solid Earth*, *124*(8), 8584–8610. https://doi.org/10.1029/2019JB017684

Weng, H., & Ampuero, J.-P. (2020). Continuum of earthquake rupture speeds enabled by oblique slip. *Nature Geoscience*, *13*(12), 817–821. https://doi.org/10.1038/s41561-020-00654-4

Xu, S., Fukuyama, E., & Yamashita, F. (2019). Robust estimation of rupture properties at propagating front of laboratory earthquakes. *Journal of Geophysical Research: Solid Earth*, *124*(1), 766–787. https://doi.org/10.1029/2018JB016797

Geophysical Research Letters

Supporting Information for

Intermittent supershear rupture punctuated by barrier-induced stopping phase during the 2025 M_w 7.8 Myanmar earthquake: Evidence from near-fault strong motion observation

Xiaotian Ding[1], Shiqing Xu[1,*], Lingling Ye[1]

[1]Department of Earth and Space Sciences, Southern University of Science and Technology, Shenzhen, China

[*]Corresponding author: xusq3@sustech.edu.cn

Contents of this file

Introduction

In this supporting information, we show the basic idea for understanding the relation between the 2.5D and 3D models (Text S1), explain the model setup for conducting numerical simulations (Text S2 to S7), present the methods for evaluating waveform fit (Text S8), and briefly summarize the contents of related figures and tables (Text S9). Several additional figures (Figures S1 to S17) and tables (Tables S1 to S2) are also included, to provide further support for the ideas and/or statements presented in the main text.

Text S1. The relation between the 2.5D and 3D models

Figure S1 shows the equivalent mapping between a 2.5D model and a conventional 3D model. The 2.5D model is similar to a conventional 2D model, featured by a 1D fault embedded in a 2D plane (the XY plane, see Fig. S1a), but can also take into account the stress communication at the vertical boundary (in Z direction) of the seismogenic zone (Weng & Ampuero, 2019, 2020). From a 3D point of view, the 2.5D model can be considered as a 2D fault plane embedded in a 3D full space, where the finite seismogenic zone width ($W_{2.5\mathrm{D}}$) can lead to a rupture transition from crack-like to pulse-like, once the along-strike rupture propagation distance exceeds some threshold value proportional to $W_{2.5\mathrm{D}}$ (Day, 1982). Since a buried earthquake on a vertical strike-slip fault (as the full-space case in Fig. S1a) can be approximated by the superposition of a surface-breaking earthquake on a similar fault (as the half-space case in Fig. S1b) and its "mirror" above the free surface (Pollard & Segall, 1987; Luo et al., 2017), it follows that there is an equivalent mapping between the seismogenic zone width in the 2.5D full-space model ($W_{2.5\mathrm{D}}$) and that in the 3D half-space model ($W_{3\mathrm{D}}$):

$$W_{2.5\mathrm{D}} = 2 \cdot W_{3\mathrm{D}} \tag{S1}$$

According to the kinematic source model of Ye et al. (2025) for subfault F3 (Fig. 1b) and the above mapping relation (Eq. S1), we choose $W_{3\mathrm{D}}$ as 7.5 km for the 3D model and $W_{2.5\mathrm{D}}$ as 15 km for the 2.5D model.

In this study, structured meshes are implemented in both the 2.5D and 3D models, as the spectral element method (SEM) is chosen to solve the dynamic rupture problem. The number of Gauss-Lobatto-Legendre (NGLL) points per element is set to 5. The element size is set as 250 m for the 2.5D model and 500 m for the 3D model, equivalent to a grid resolution of ~ 62.5 m and ~ 125 m, respectively. The Courant–Friedrichs–Lewy (CFL) number is set to 0.50 for the 2.5D model and 0.13 for the 3D model, resulting in timesteps of 0.0039 s and 0.00125 s, respectively. The 2.5D model domain extends 250 km in the strike direction ($\mathrm{X} \in [-100\ \mathrm{km}, 150\ \mathrm{km}]$) and 150 km in the fault-normal direction ($\mathrm{Y} \in [-75\ \mathrm{km}, 75\ \mathrm{km}]$). The 3D model extends the same 250 km in the strike direction ($\mathrm{X} \in [-100\ \mathrm{km}, 150\ \mathrm{km}]$), 80 km in the fault-normal direction ($\mathrm{Y} \in [-40\ \mathrm{km}, 40\ \mathrm{km}]$), and 40 km in the depth direction ($\mathrm{Z} \in [-40\ \mathrm{km}, 0]$). For convenience, later we use non-negative

values for discussing depth in the 3D model (as in Fig. S2). Absorbing boundary conditions are applied to all surrounding boundaries, except for the free surface in the 3D model (Fig. S1b), which is treated with a traction-free boundary condition.

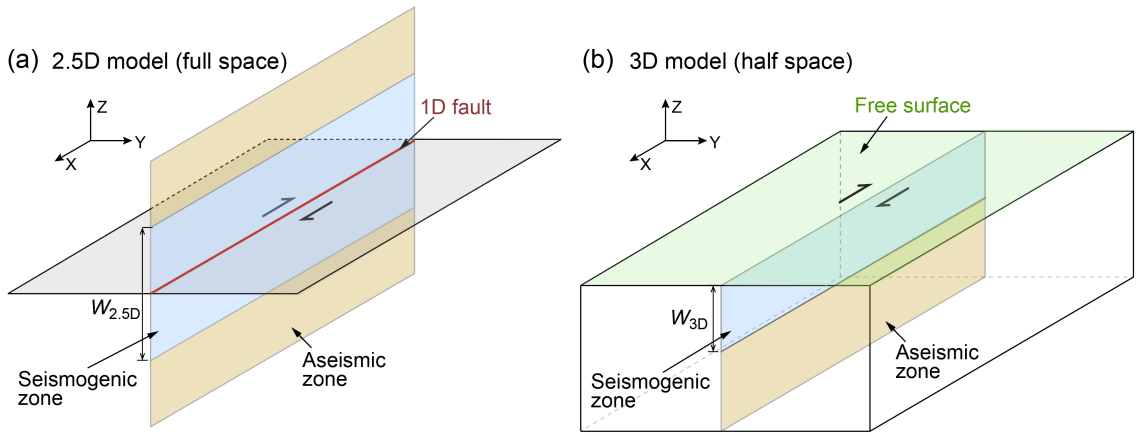

Figure S1. Schematic illustration of the relation between (a) a 2.5D model in full space and (b) a 3D model in half space. For (a) and (b), a vertical strike-slip fault is considered, with blue area and yellow area representing the seismogenic zone and aseismic zone, respectively, and $W_{2.5D}$ and W_{3D} indicating the corresponding seismogenic zone width. In (a), red line indicates a 1D fault embedded in a 2D plane (in gray). In (b), the free surface is colored in green.

Text S2. Elastic properties

Proper setup of elastic properties in numerical simulations is crucial for comparing simulated waveforms with data. Here, we estimate the related values based on the regional velocity structure for Myanmar (Shiddiqi et al., 2019). After some averaging over the seismogenic depth, P wave speed (C_P) and S wave speed (C_S) are set as $5580\ \mathrm{m/s}$ and $3310\ \mathrm{m/s}$, respectively. Subsequently, Rayleigh wave speed (C_R) is estimated as $3031\ \mathrm{m/s}$ following Aki and Richards (2002), and mass density (ρ) is empirically determined as $2633\ \mathrm{kg/m^3}$ following Brocher (2005). For simplicity, we don't consider any spatial variations of elastic properties in the current simulations, such as a material contrast across the Sagaing fault, a sedimentary basin in the top few kilometers, or a fault damage zone with reduced wave speeds (Peng et al., 2025). These complexities are left for the future work aiming to simulate more realistic ground motions.

Text S3. Friction laws

As in Ding et al. (2023), a time-weakening friction (TWF) law is used to artificially nucleate the rupture on the modeled subfault F3, by forcing friction coefficient f to drop with time t at a constant rate of $(f_\mathrm{s} - f_\mathrm{d}) \cdot V_\mathrm{r}^\mathrm{TWF}/L_0$:

$$f = \min\left\{\max\left\{f_0 - \frac{(f_\mathrm{s}-f_\mathrm{d})\cdot(V_\mathrm{r}^\mathrm{TWF}\cdot t - r)}{L_0}, f_\mathrm{d}\right\}, f_\mathrm{s}\right\} \tag{S2}$$

where f_0 is the initial shear-to-normal stress ratio ($\sigma_\mathrm{xy}^\mathrm{i}/\left|\sigma_\mathrm{yy}^\mathrm{i}\right|$, to be introduced in Text S4), f_s and f_d are the static and dynamic friction coefficient, respectively, $V_\mathrm{r}^\mathrm{TWF}$ is a constant speed at which rupture is forced to propagate, r is the distance from the nucleation site on subfault F3.

After a certain amount of propagation distance, a slip-weakening friction (SWF) law will take over the control, with friction coefficient f linearly decreasing with slip δ until reaching a critical value D_c:

$$f = \begin{cases} f_\mathrm{s} - (f_\mathrm{s} - f_\mathrm{d}) \cdot \frac{\delta}{D_\mathrm{c}}, & \text{if } \delta \le D_\mathrm{c} \\ f_\mathrm{d}, & \text{if } \delta > D_\mathrm{c} \end{cases} \tag{S3}$$

where f_s and f_d retain the same meanings and values as those in TWF. Accordingly, static and dynamic strength can be defined as $\tau_\mathrm{s} = f_\mathrm{s} \cdot |\sigma_\mathrm{n}|$ and $\tau_\mathrm{d} = f_\mathrm{d} \cdot |\sigma_\mathrm{n}|$, respectively, with $|\sigma_\mathrm{n}|$ being the magnitude of normal stress (see Text S4, S5 and S7). Under the control of SWF, rupture can propagate spontaneously with a varying rupture speed. In most cases, we use the above strategy involving both TWF and SWF to simulate a variety of rupture speeds approaching the target NPW station on subfault F3. In some other cases, we employ TWF only but with different constant speeds (with respect to $\sqrt{2}C_\mathrm{S}$) to explore the corresponding wavefield under a (quasi)steady-state supershear rupture.

Text S4. Basic setup of the initial stress field

The fundamental part of the initial stress field, in the absence of any further model complexities, is set based on the previous modeling works on strike-slip earthquakes (Dunham & Archuleta, 2004; Ding et al., 2023) as well as trial-and-error specifically made for the 2025 Myanmar earthquake. Without losing generality, initial normal stress ($\sigma_\mathrm{yy}^\mathrm{i}$) is set at -50 MPa (negative for compression) and strike-parallel initial shear stress ($\sigma_\mathrm{xy}^\mathrm{i}$) is

set at 24 MPa in the 2.5D model. In the 3D model, dip-parallel initial shear stress (σ_{yz}^{i}) is chosen as 0 MPa at all depths, while σ_{yy}^{i} and σ_{xy}^{i} are assumed to linearly taper toward zero over the uppermost 1 km (Fig. S2a), to ensure a close similarity with the 2.5D model over much of the seismogenic zone and a compatibility with the free surface condition as assumed in previous studies (Ma, 2008; Kaneko & Lapusta, 2010).

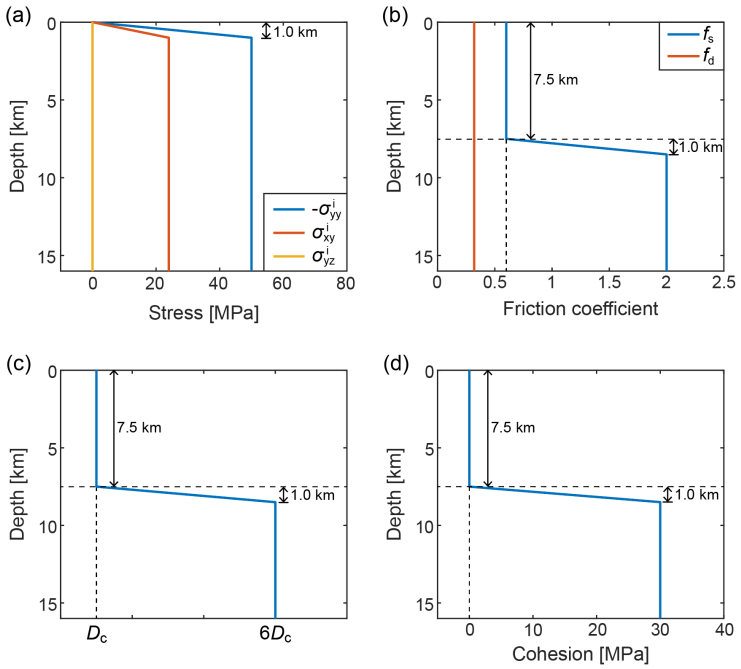

Figure S2. Additional setup for the 3D model. (a) Along-depth distribution of various stress components. (b) Along-depth distribution of static and dynamic friction coefficient. (c) Along-depth distribution of slip-weakening distance, expressed by the basic unit of D_c used in the 2.5D model. (d) Along-depth distribution of fault cohesion. Except for the stress field in the uppermost 1 km, all the parameters above the depth of 7.5 km share the same values as in the 2.5D model. For (a)-(d), positive depth corresponds to the negative direction along the Z-axis (see Fig. S1).

Text S5. Setup of the seismogenic zone

While the seismogenic zone can be directly defined via the parameter $W_{2.5D}$ in the 2.5D model (Fig. S1a), it needs to be manually set in the 3D model. Here for the 3D model, the down-dip transition from the seismogenic zone to the aseismic zone (Fig. S1b) is realized by assigning increased-then-saturated values of static friction coefficient (f_s) (Fig. S2b), slip-weakening distance ($D_c \rightarrow 6D_c$) (Fig. S2c) and fault cohesion (the intrinsic part of fault

strength that is independent of normal stress) below the depth of 7.5 km (Fig. S2d). The assumed values have been tested to be strong enough to restrict the simulated 3D ruptures in the top 7.5 km or so.

Text S6. Additional setup for promoting/arresting rupture toward the south/north

In order to simulate dynamic ruptures with different speeds, we follow the method of Dunham and Archuleta (2004) to introduce an asperity to the south of rupture nucleation site on subfault F3 (different from the actual hypocenter on subfault F1). The asperity is realized by increasing initial (strike-parallel) shear stress τ_i from 24 MPa toward a constant higher level of τ_i^{Asp}, with a purpose to promote rupture acceleration including possible supershear transition toward the south. The exact value of τ_i^{Asp} varies from case to case, and will be tuned to control the rupture speed and the slip pulse amplitude approaching the target NPW station. On the opposite side, static friction coefficient f_s is assumed to rise from 0.6 toward 5.0, in order to impede rupture propagation toward the north (not the focus of current study). It should be noted that the above methods for promoting or arresting rupture propagation are arbitrary. The main purpose is to output a southward-propagating rupture, whose wavefield can be checked with the observation at the NPW station, rather than to reproduce precisely the inverted rupture process on subfault F3 (Ye et al., 2025).

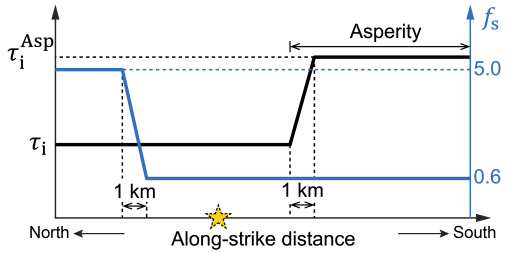

Figure S3. Additional setup of initial shear stress τ_i and static friction coefficient f_s. τ_i (in black) is assumed to increase and then saturate at a higher level τ_i^{Asp} toward the south, in order to promote rupture propagation in this direction. f_s (in blue) is assumed to exhibit a similar behavior but toward the north, in order to arrest rupture in this direction. The region with increased τ_i is referred to as an asperity. Yellow pentagram indicates rupture nucleation site on the modeled subfault F3, which is set arbitrarily and should not be mixed with the actual observation.

Text S7. Realization of a barrier near the NPW station

We try three different ways to model a barrier near the NPW station: a fault patch with (a) spatially decreased initial shear stress (τ_{i}) (Fig. S4a), (b) spatially increased magnitude of initial normal stress ($|\sigma_{\mathrm{n}}| = |\sigma_{\mathrm{yy}}^{\mathrm{i}}|$) (Fig. S4b), and (c) spatially increased static friction coefficient (f_{s}) (Fig. S4c). For all the three, the related quantity first deviates from its original level by a constant gradient, but later remains at a new, constant level after a certain along-strike distance. We use the related gradient of initial shear stress $\nabla\tau_{\mathrm{i}}$ or that of static strength $\nabla\tau_{\mathrm{s}} = \nabla(f_{\mathrm{s}} \cdot |\sigma_{\mathrm{n}}|)$ to assess the effect of barrier strength. In addition, we also examine the effect of barrier location, defined by the relative distance of its starting position to the NPW station ($\mathrm{X}_{\mathrm{Bar-NPW}}$). $\mathrm{X}_{\mathrm{Bar-NPW}}$ is positive and negative when the barrier is located on the southern and northern side of the NPW station, respectively.

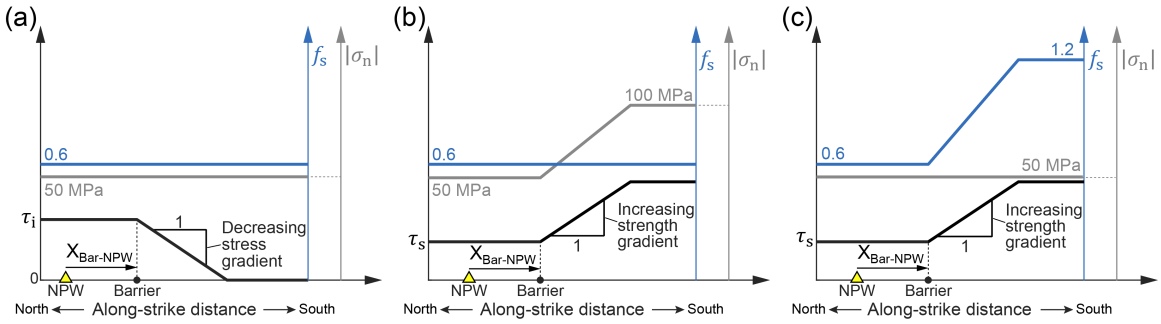

Figure S4. Realization of a fault barrier near the NPW station, associated with (a) spatially decreased initial shear stress τ_{i}, (b) spatially increased initial normal stress $|\sigma_{\mathrm{n}}|$, and (c) spatially increased static friction coefficient f_{s}. Decreasing stress gradient and increasing strength gradient are evaluated by $\nabla\tau_{\mathrm{i}}$ and $\nabla\tau_{\mathrm{s}} = \nabla(f_{\mathrm{s}} \cdot |\sigma_{\mathrm{n}}|)$, respectively. $\mathrm{X}_{\mathrm{Bar-NPW}}$ defines the starting position of the barrier relative to the NPW station, with positive/negative indicating the barrier on the southern/northern side of the NPW station.

Text S8. Methods for evaluating waveform fit

A metric in terms of root-mean-square-error (RMSE) is introduced to evaluate the similarity between the simulated synthetic waveform and the observed one. A lower RMSE value indicates a higher similarity between the two and hence a better waveform fit. The core steps for evaluating waveform fit via RMSE are summarized below, following and modifying the methods in Xu et al. (2019):

Step 1: Resample the synthetic waveform under the 2.5D or 3D model from its original timestep (see Text S1) to a new one of 0.01 s, in order to match the sampling rate of the observation (100 Hz) (Lai et al., 2025).

Step 2: Cut the observed waveform in a shorter time window and the synthetic one in a longer time window. Then pick a starting point of the longer synthetic waveform.

Step 3: Use the observed waveform as a template to slide against the synthetic one, and compute the related RMSE (Eq. S4) over the time window of Stage-I to III (see Fig. 1c; we purposely ignore Stage-IV since our current simulations cannot reproduce the enduring oscillations behind the main pulse; however, we include Stage-I since this part is crucial for baseline alignment of the velocity waveform):

$$\mathrm{RMSE} = \sqrt{\frac{\sum_{i=1}^{2 \text{ or } 3} \sum_{j=1}^{N_t} \left(V_{ij}^{\mathrm{syn}} - V_{ij}^{\mathrm{obs}}\right)^2}{(2 \text{ or } 3) \cdot N_t}} \tag{S4}$$

where V_{ij}^{syn} is the extracted part of synthetic waveform, V_{ij}^{obs} is the observed waveform, and N_t is the total number of samples during Stage-I to III. The index i denotes the waveform component, corresponding to FP and FN for the 2.5D model, and FP, FN, and UD for the 3D model. Similarly, a sub-RMSE for each component, taking FP as an example ($i = 1$), can be computed:

$$\mathrm{RMSE\_FP} = \sqrt{\frac{\sum_{j=1}^{N_t} \left(V_{1j}^{\mathrm{syn}} - V_{1j}^{\mathrm{obs}}\right)^2}{N_t}} \tag{S5}$$

where V_{1j}^{syn} and V_{1j}^{obs} represent the corresponding FP component of the synthetic and observed waveforms, respectively. After the above operation, store the computed values of RMSE and sub-RMSE.

Step 4: Shift the starting point of the longer synthetic waveform by one timestep (0.01 s) and repeat Step 3, until reaching the end of synthetic waveform.

Step 5: Evaluate the distribution of RMSE as a function of shifted number of timestep. The one with a minimal value of RMSE (Fig. S5a) will be used to show the corresponding waveform fit for each component, and the associated values of RMSE_FP and RMSE_FN (Fig. S5b).

Later, when constructing the phase diagram such as in Fig. 3d, we repeat the above steps for each combination of model parameters, and plot the obtained value of RMSE (from Step 5) in the parameter space. After exploring a range of model parameters, we choose the preferred cases as those "interior points" (i.e., not at the boundary) with lower (not necessarily the lowest) values of RMSE.

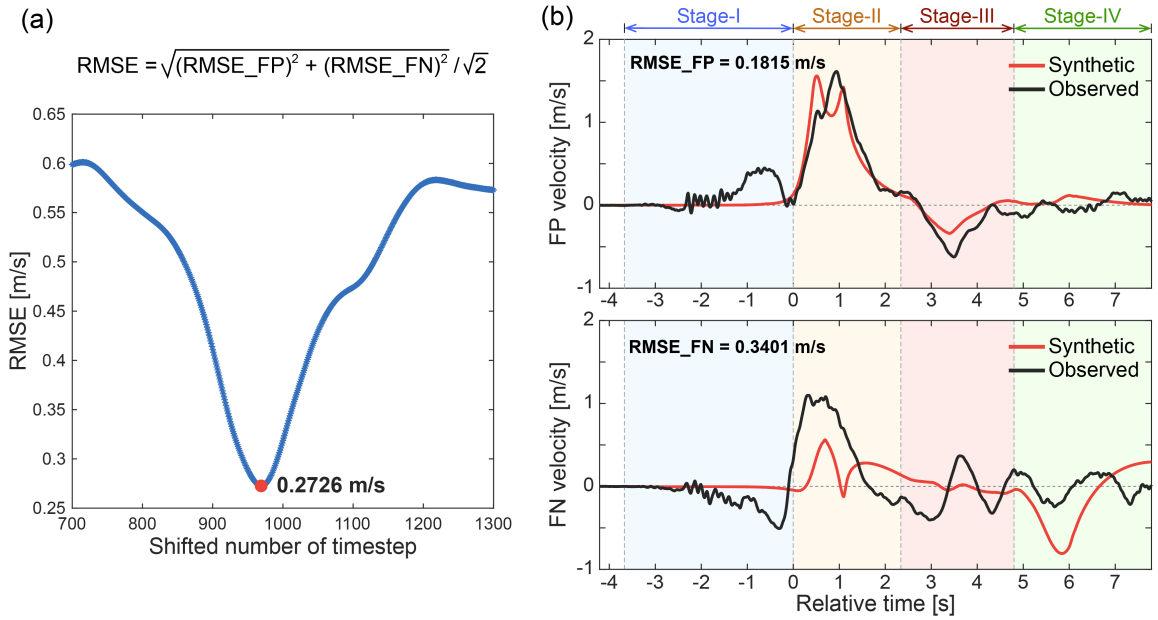

Figure S5. (a) Distribution of root-mean-square-error (RMSE) as a function of shifted number of timestep. RMSE, defined in Eq. (S4), is a metric for evaluating the general similarity between synthetic and observed waveforms over all components (here over the FP and FN components). (b) The corresponding waveforms when RMSE (evaluated over Stage-I to III) reaches a minimum (the red dot in panel (a)). RMSE_FP (Eq. S5) and RMSE_FN indicates a sub version of RMSE for the FP and FN component, respectively.

Text S9. Summary

Figures S6–S17 show additional simulation results to support various statements made in the main text (Figs. S6–S14 under the 2.5D model, and Figs. S15–S17 under the 3D model):

waveform fits under a simulated subshear rupture (Fig. S6), a simulated incipient supershear rupture (Fig. S7) and six simulated (quasi)steady-state supershear ruptures (Fig. S8), comparison between on-fault slip velocity and off-fault particle velocity (Fig. S9), effect of barrier location on waveform fit (Figs. S10 and S11), effect of barrier strength on waveform fit (Fig. S12), preferred cases with barrier realized by increased normal stress and the related phase diagrams (Fig. S13), preferred cases with barrier realized by increased static friction coefficient and the related phase diagrams (Fig. S14), and selected preferred cases under the 3D model (Figs. S15–S17).

Table S1 summarizes the basic parameters and their values, common for both the 2.5D and 3D models (excluding those for the aseismic zone in the 3D model). Table S2 lists the specific parameter values used in some simulation cases, without or with a fault barrier.

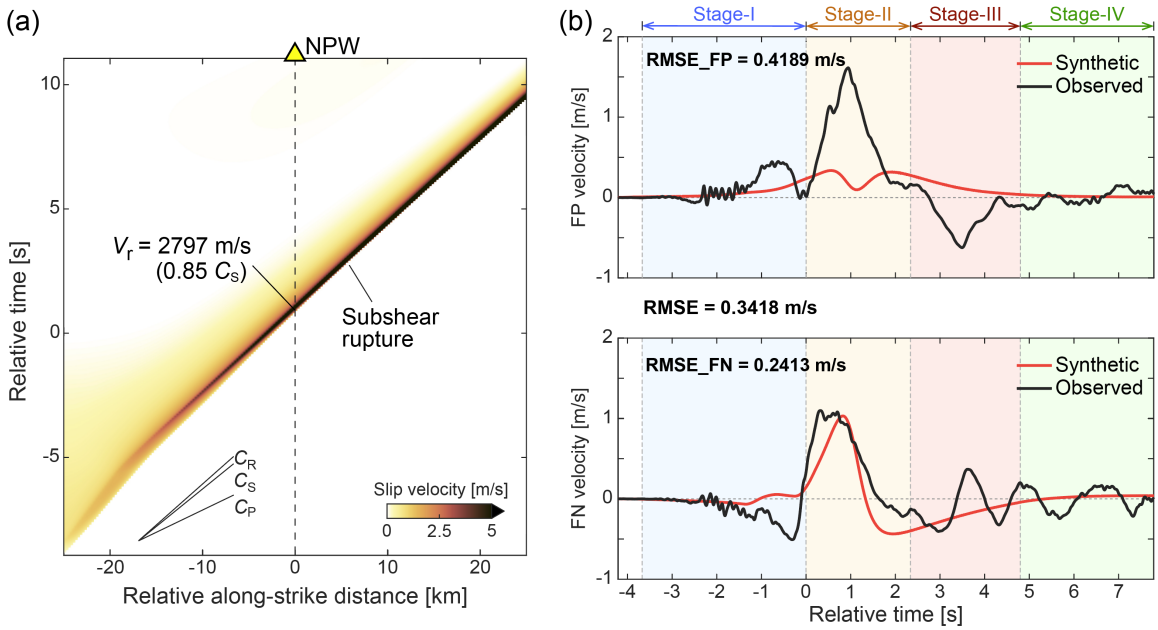

Figure S6. (a) Evolution of slip velocity for a simulated subshear rupture under the 2.5D model. (b) The related waveform fit with data at the NPW station. See Text S8 and Fig. S5 for the meanings and computations of RMSE, RMSE_FP and RMSE_FN.

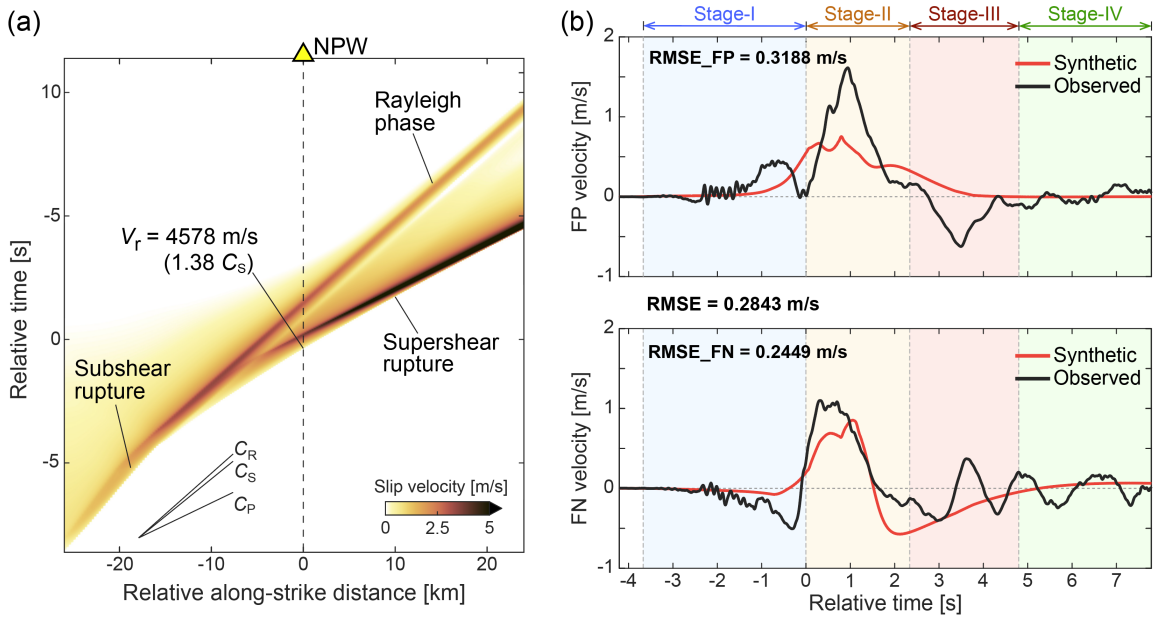

Figure S7. Similar to Figure S6, but for an incipient supershear rupture that has just transitioned from subshear near the NPW station.

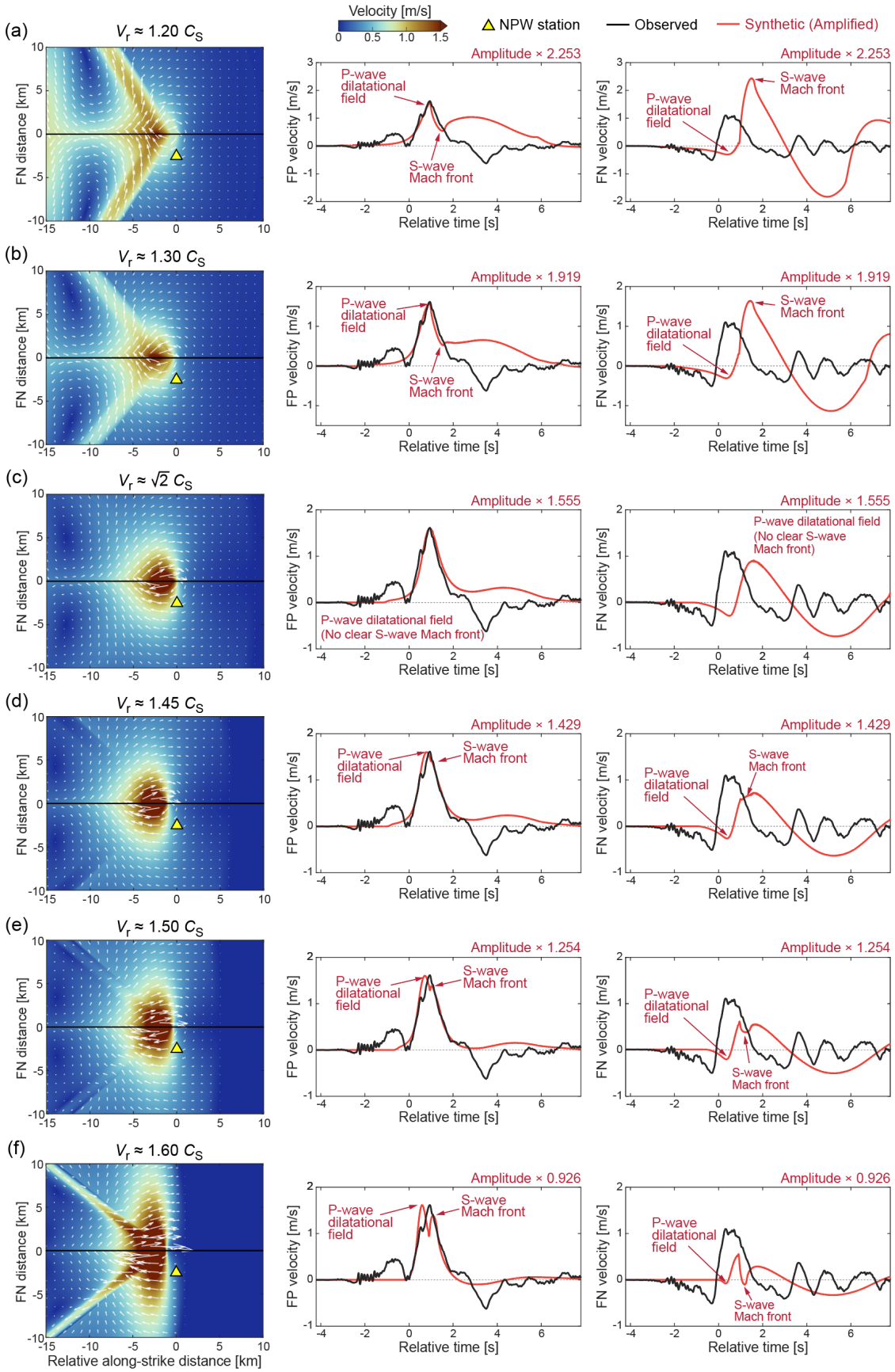
Velocity [m/s]
0 0.5 1.0 1.5
NPW station
Observed
Synthetic (Amplified)
(a)
$V_r \approx 1.20\ C_S$
Amplitude × 2.253
(b)
$V_r \approx 1.30\ C_S$
Amplitude × 1.919
(c)
$V_r \approx \sqrt{2}\ C_S$
Amplitude × 1.555
(d)
$V_r \approx 1.45\ C_S$
Amplitude × 1.429
(e)
$V_r \approx 1.50\ C_S$
Amplitude × 1.254
(f)
$V_r \approx 1.60\ C_S$
Amplitude × 0.926
FN distance [km]
FP velocity [m/s]
FN velocity [m/s]
Relative time [s]
Relative along-strike distance [km]
P-wave dilatational field
S-wave Mach front
P-wave dilatational field (No clear S-wave Mach front)

Figure S8. (a)-(f) Simulated wavefields for six (quasi)steady-state supershear ruptures under the control of time-weakening friction (TWF) in the 2.5D model (first column), and the related waveform comparison with the observation at the NPW station (second and third columns). In the first column, rupture propagates to the "right" (south), with background color showing the magnitude of particle velocity and white arrows indicating the direction and relative magnitude of particle motion. Positive FP in the second column and positive FN in the third column correspond to the "left" and "up" in the first column, respectively.

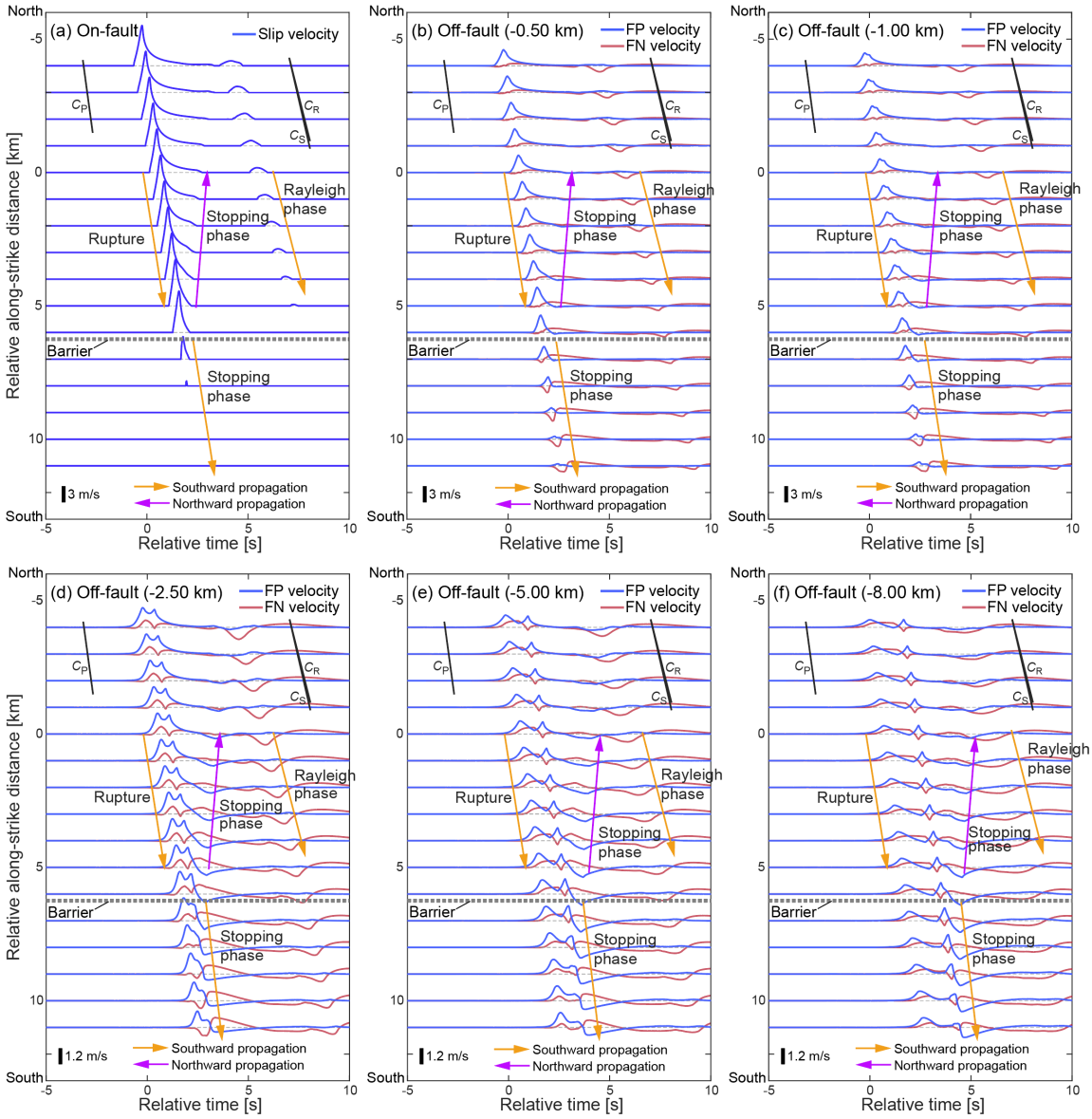

Figure S9. Evolutions of simulated on-fault slip velocity (a) and off-fault particle velocity (b-f) at a series of along-strike distances or off-fault distances. The results here correspond to the case shown in Figs. 3a and 3b.

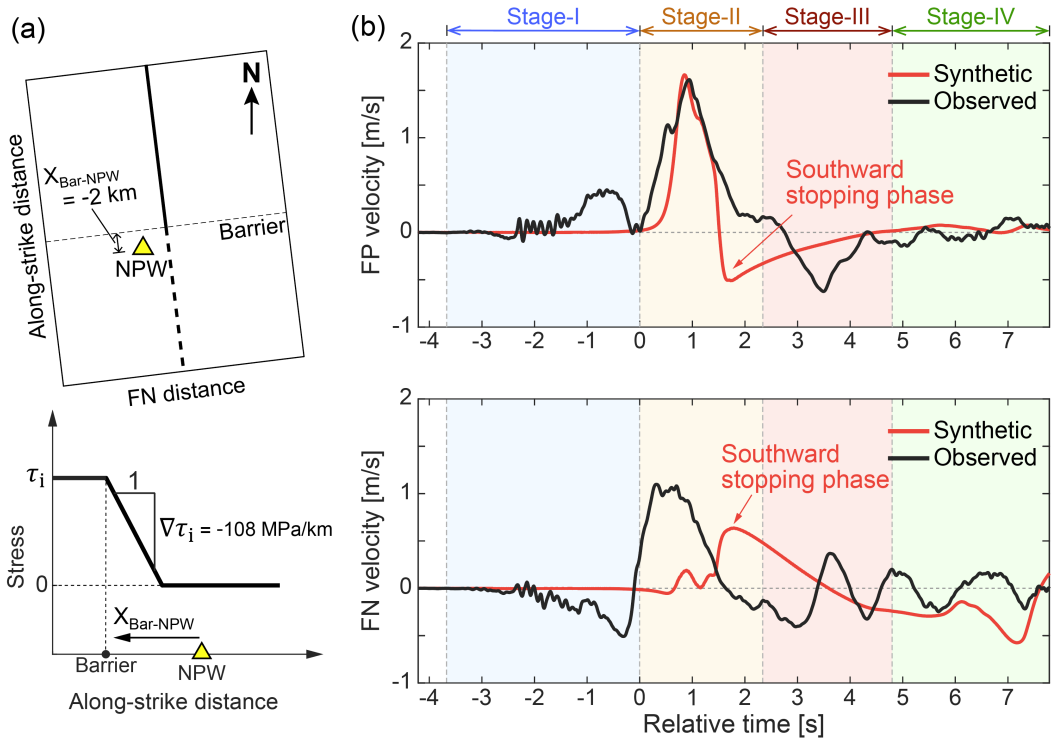

Figure S10. Similar to Figs. 3a and 3b, but with a barrier located on the northern side of the NPW station ($X_{Bar-NPW} = -2$ km, instead of the previous value of 6.25 km). For this case, the simulated negative FP pulse (in red) reflects the southward-propagating part of the stopping phase (for reference, see the simulated wavefield in Fig. 3a or the waveforms in Fig. S9).

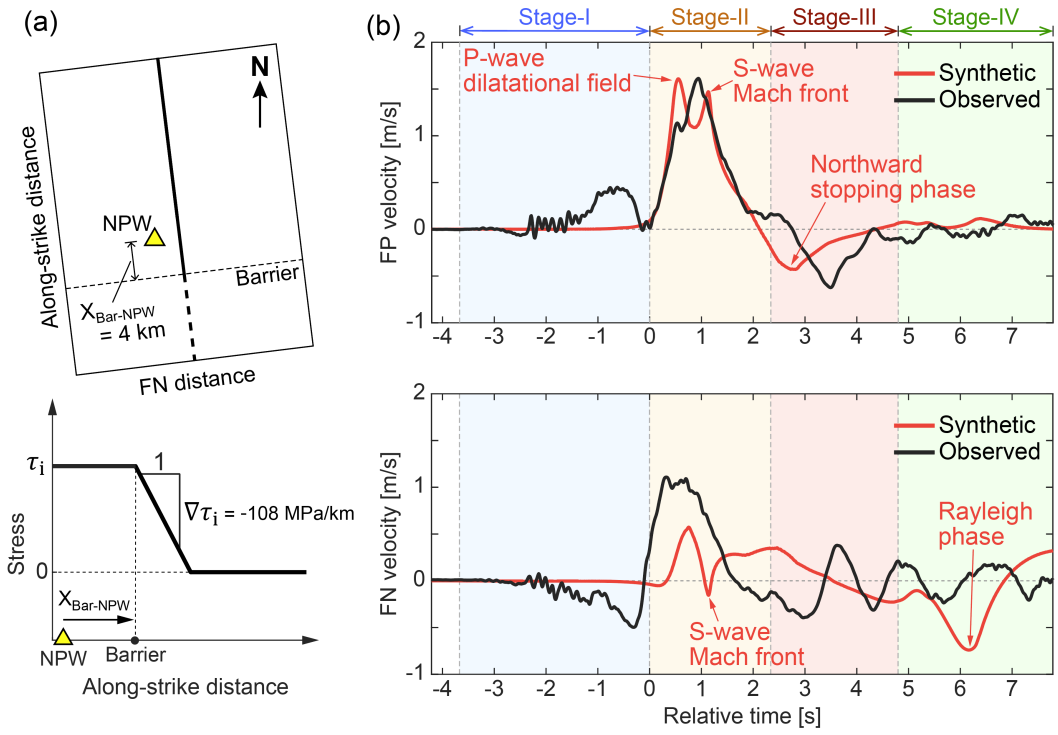

Figure S11. Similar to Figs. 3a and 3b, but with a barrier located closer to the NPW station on its southern side ($X_{Bar-NPW} = 4$ km, instead of the previous value of 6.25 km). For this case, the simulated negative FP pulse (in red) arrives earlier than the observed one (in black).

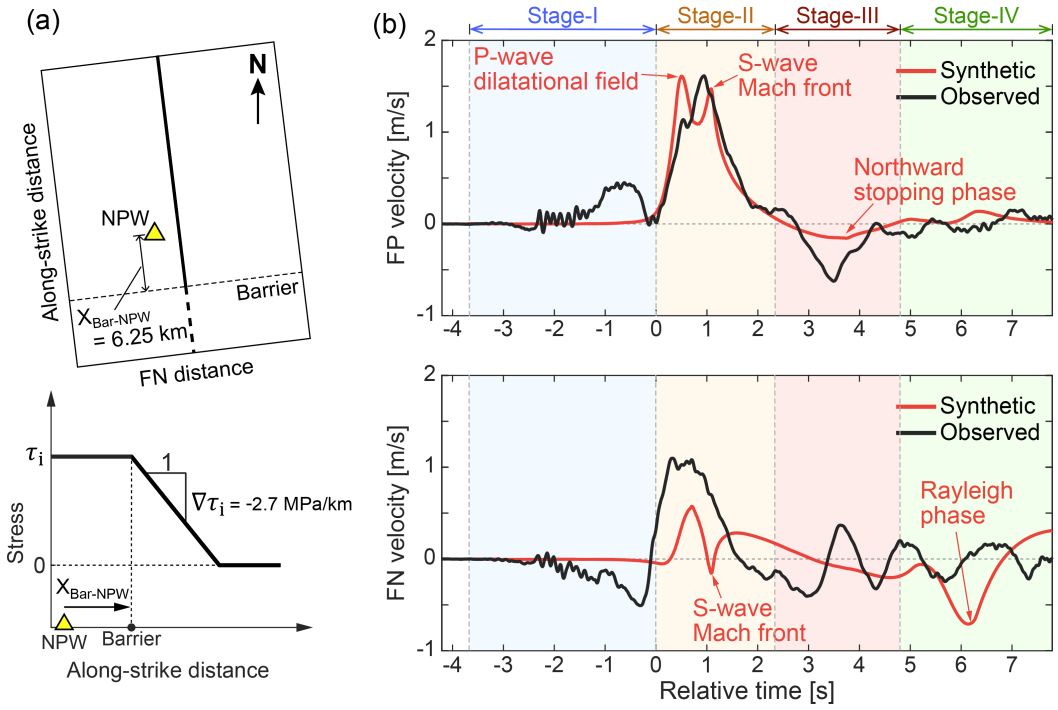

Figure S12. Similar to Figs. 3a and 3b, but with a weaker barrier ($\nabla\tau_i = -2.7$ MPa/km, instead of the previous value of -108 MPa/km). For this case, the amplitude of the simulated negative FP pulse (in red) is much reduced.

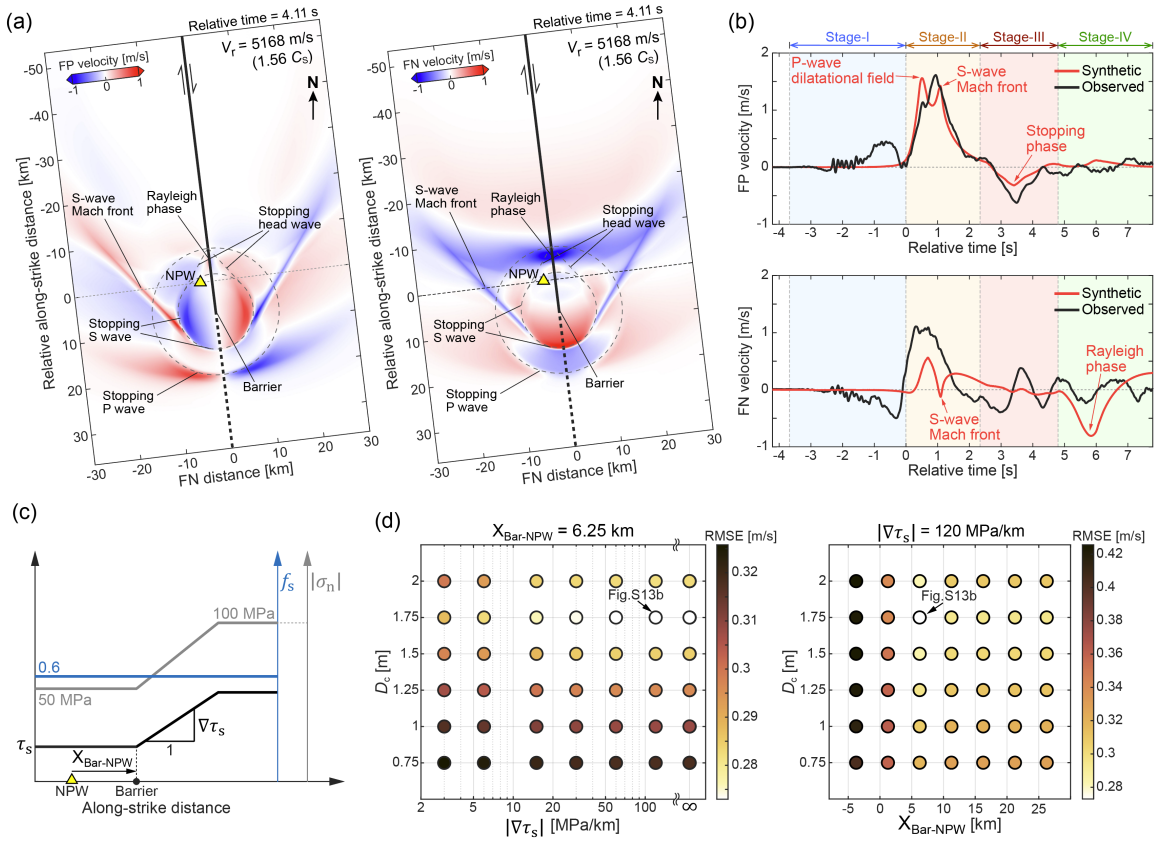

Figure S13. Similar to Fig. 3, but with the barrier realized by a spatial increase of initial normal stress $|\sigma_n|$ and hence static strength $\tau_s = f_s \cdot |\sigma_n|$. Here $\nabla\tau_s$ represents increasing strength gradient (Text S7, Fig. S4b).

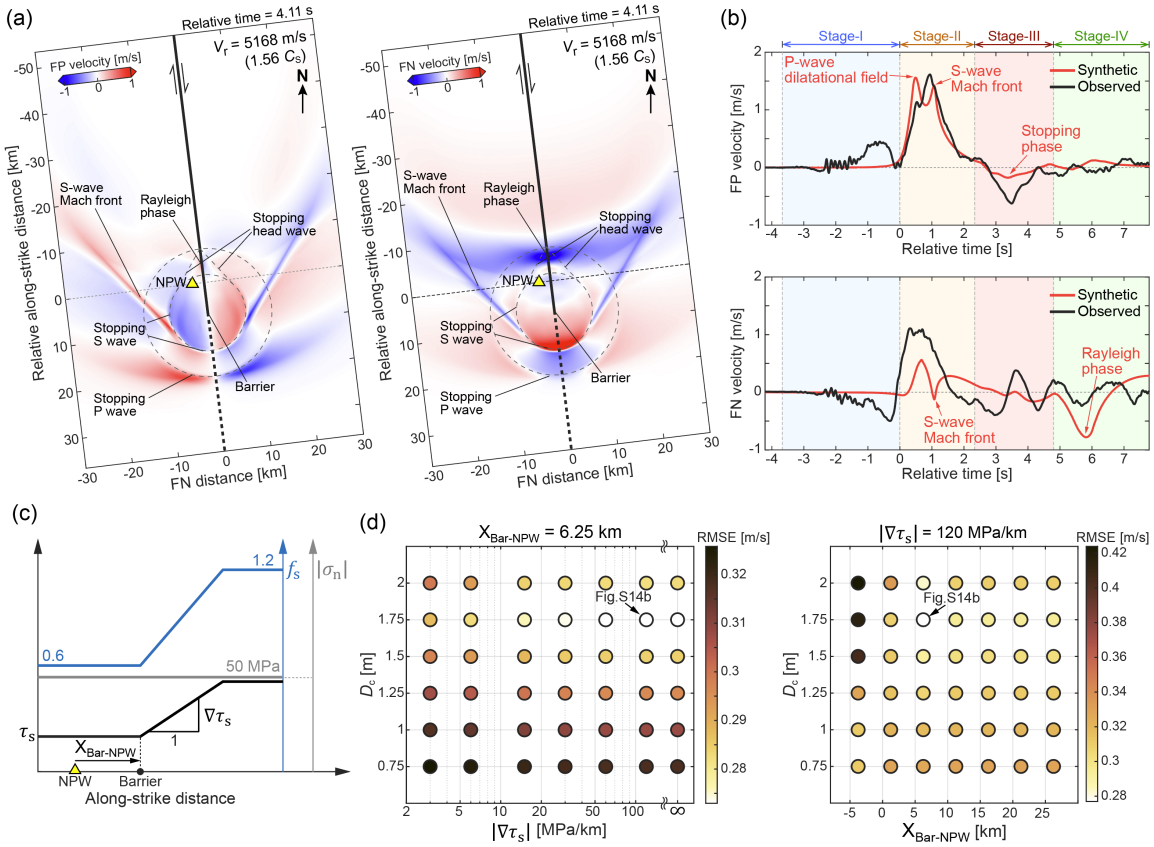

Figure S14. Similar to Fig. 3, but with the barrier realized by a spatial increase of static friction coefficient f_s and hence static strength $\tau_s = f_s \cdot |\sigma_n|$. Here $\nabla\tau_s$ represents increasing strength gradient (Text S7, Fig. S4c).

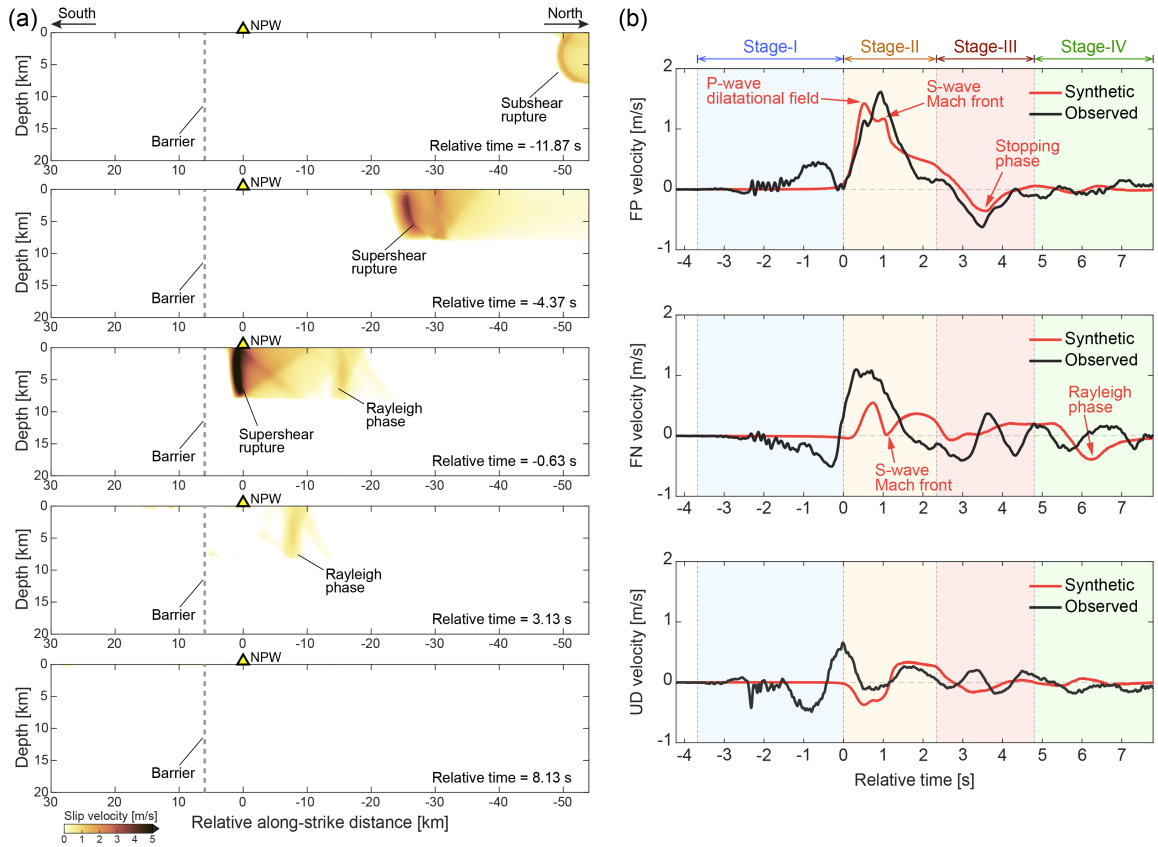

Figure S15. (a) Simulated slip velocity evolution for a barrier-impeded supershear rupture under the 3D model. (b) The related waveform fit with data at the NPW station. For this case, the barrier is realized by a spatial decrease of initial shear stress (see Table S2 for more information).

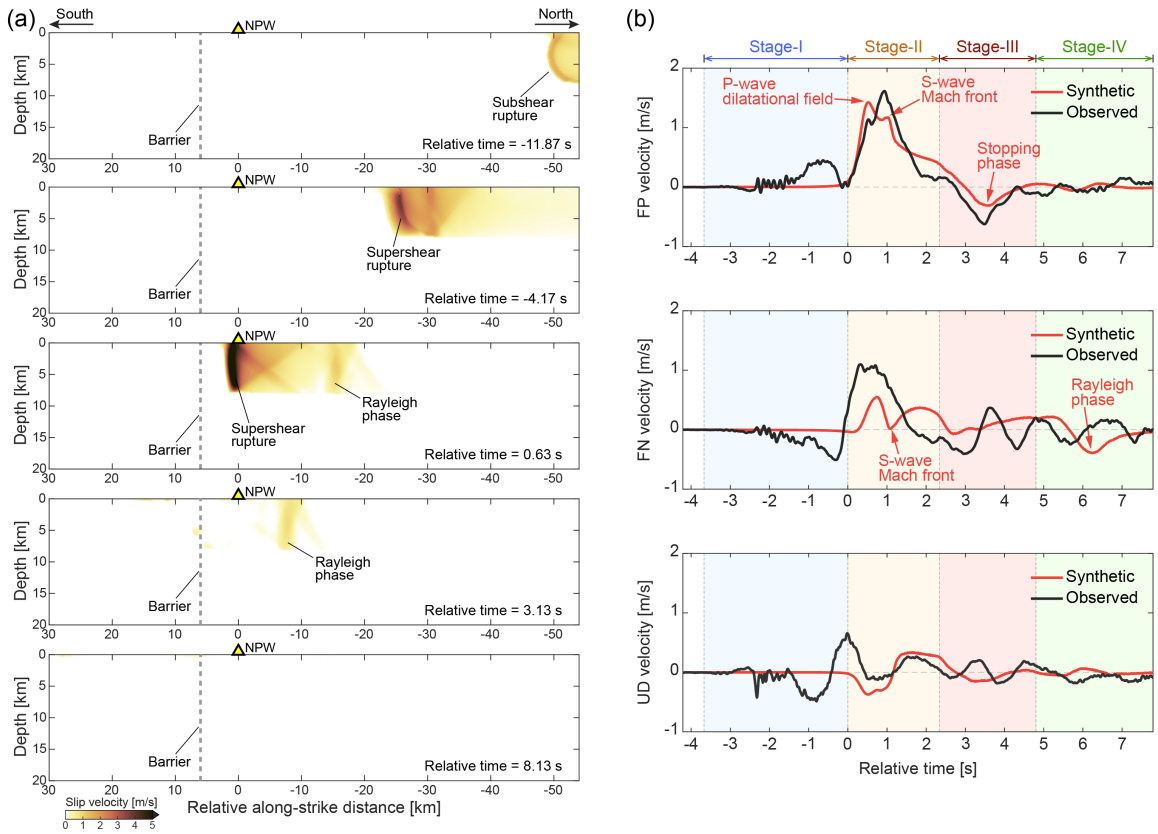

Figure S16. Similar to Fig. S15, but with the barrier realized by a spatial increase of initial normal stress (see Table S2 for more information).

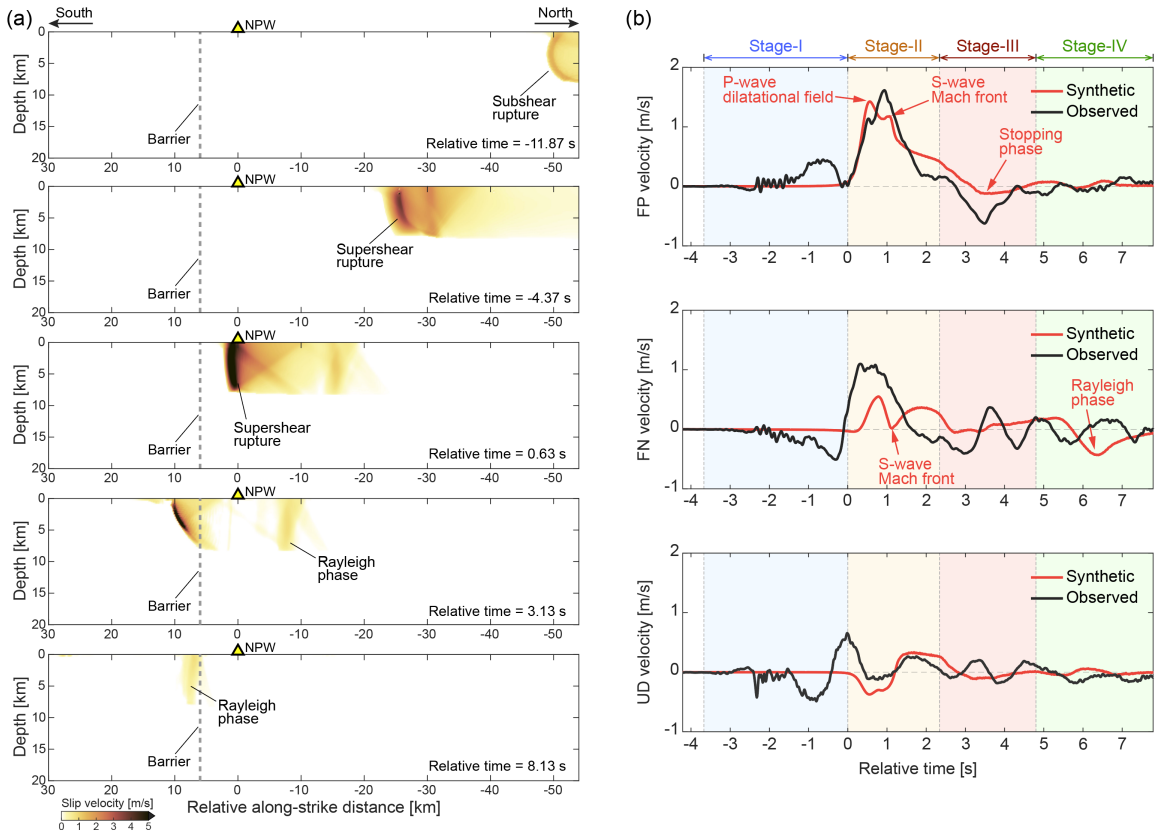

Figure S17. Similar to Fig. S15, but with the barrier realized by a spatial increase of static friction coefficient (see Table S2 for more information).

Table S1. Basic parameters and their values

Parameters	Values
P wave speed (C_{P})	$5580\ \mathrm{m/s}$
S wave speed (C_{S})	$3310\ \mathrm{m/s}$
Rayleigh wave speed (C_{R})	$3031\ \mathrm{m/s}$
Mass density (ρ)	$2633\ \mathrm{kg/m^3}$
Static friction coefficient (TWF & SWF) (f_{s})	0.60
Dynamic friction coefficient (TWF & SWF) (f_{d})	0.32
Rupture propagation speed (TWF, most cases) ($V_{\mathrm{r}}^{\mathrm{TWF}}$)	$2000\ \mathrm{m/s}$
Characteristic length (TWF) (L_0)	$2\ \mathrm{km}$
Slip-weakening distance (SWF) (D_{c})	$(0.75 — 2.00)\ \mathrm{m}$
Initial normal stress ($\sigma_{\mathrm{n}} = \sigma_{\mathrm{yy}}^{\mathrm{i}}$)	$-50\ \mathrm{MPa}$
Initial strike-parallel shear stress (non-asperity) ($\tau_{\mathrm{i}} = \sigma_{\mathrm{xy}}^{\mathrm{i}}$)	$24\ \mathrm{MPa}$
Initial dip-parallel shear stress ($\sigma_{\mathrm{yz}}^{\mathrm{i}}$)	$0\ \mathrm{MPa}$
Initial strike-parallel shear stress (asperity) ($\tau_{\mathrm{i}} = \tau_{\mathrm{i}}^{\mathrm{Asp}}$)	$(24.50 — 27.00)\ \mathrm{MPa}$

Table S2. Certain parameters and their values used in specific cases

Figure #	Parameters	Values
Figs. 2a and 2b	Slip-weakening distance (D_c)	0.75 m
	Initial strike-parallel shear stress (asperity) (τ_i^{Asp})	25.75 MPa
Figs. 2c and 2d	Slip-weakening distance (D_c)	1.75 m
	Initial strike-parallel shear stress (asperity) (τ_i^{Asp})	27.00 MPa
Figs. 3a, 3b, 4, S5, S9, S10, and S11	Slip-weakening distance (D_c)	1.75 m
	Initial strike-parallel shear stress (asperity) (τ_i^{Asp})	27.00 MPa
	Magnitude of decreasing stress gradient ($\lvert\nabla\tau_i\rvert$)	108 MPa/km
Fig. S6	Slip-weakening distance (D_c)	1.25 m
	Initial strike-parallel shear stress (asperity) (τ_i^{Asp})	24.50 MPa
Fig. S7	Slip-weakening distance (D_c)	1.25 m
	Initial strike-parallel shear stress (asperity) (τ_i^{Asp})	26.00 MPa
Fig. S12	Slip-weakening distance (D_c)	1.75 m
	Initial strike-parallel shear stress (asperity) (τ_i^{Asp})	27.00 MPa
	Magnitude of decreasing stress gradient ($\lvert\nabla\tau_i\rvert$)	2.7 MPa/km
Figs. S13 and S14	Slip-weakening distance (D_c)	1.75 m
	Initial strike-parallel shear stress (asperity) (τ_i^{Asp})	27.00 MPa
	Magnitude of increasing strength gradient ($\lvert\nabla\tau_s\rvert$)	120 MPa/km
Fig. S15	Slip-weakening distance (D_c)	1.25 m
	Initial strike-parallel shear stress (asperity) (τ_i^{Asp})	27.00 MPa
	Magnitude of decreasing stress gradient ($\lvert\nabla\tau_i\rvert$)	54 MPa/km
Figs. S16 and S17	Slip-weakening distance (D_c)	1.25 m
	Initial strike-parallel shear stress (asperity) (τ_i^{Asp})	27.00 MPa
	Magnitude of increasing strength gradient ($\lvert\nabla\tau_s\rvert$)	60 MPa/km

References From the Supporting Information

Aki, K., & Richards, P. G. (2002). *Quantitative seismology* (2nd Ed.). Mill Valley, CA: University Science Books.

Brocher, T. M. (2005). Empirical relations between elastic wavespeeds and density in the earth's crust. *Bulletin of the Seismological Society of America*, 95(6), 2081–2092. https://doi.org/10.1785/0120050077

Day, S. (1982). Three-dimensional finite difference simulation of fault dynamics: Rectangular faults with fixed rupture velocity. *Bulletin of the Seismological Society of America*, 72(3), 705–727. https://doi.org/10.1785/BSSA0720030705

Dunham, E. M., & Archuleta, R. J. (2004). Evidence for a supershear transient during the 2002 Denali fault earthquake. *Bulletin of the Seismological Society of America*, 94(6B), S256–S268. https://doi.org/10.1785/0120040616

Kaneko, Y., & Lapusta, N. (2010). Supershear transition due to a free surface in 3-D simulations of spontaneous dynamic rupture on vertical strike-slip faults. *Tectonophysics*, 493(3–4), 272–284. https://doi.org/10.1016/j.tecto.2010.06.015

Luo, Y., Ampuero, J.-P., Miyakoshi, K., & Irikura, K. (2017). Surface rupture effects on earthquake moment-area scaling relations. *Pure and Applied Geophysics*, 174, 3331–3342. https://doi.org/10.1007/s00024-017-1467-4

Ma, S. (2008). A physical model for widespread near-surface and fault zone damage induced by earthquakes. *Geochemistry, Geophysics, Geosystems*, 9(11), Q11009, https://doi.org/10.1029/2008GC002231

Pollard, D. D., & Segall, P. (1987). Theoretical displacements and stresses near fractures in rock: With applications to faults, joints, veins, dikes, and solution surfaces. In Atkinson, B. K. (Ed.), *Fracture mechanics of rock* (Chap. 8, pp. 277–349). London: Academic Press. https://doi.org/10.1016/b978-0-12-066266-1.50013-2

Shiddiqi, H. A., Tun, P. P., & Ottemöller, L. (2019). Minimum 1D velocity model and local magnitude scale for Myanmar. *Seismological Research Letters*, 90(5), 1923–1936. https://doi.org/10.1785/0220190065

Weng, H., & Ampuero, J.-P. (2019). The dynamics of elongated earthquake ruptures. *Journal of Geophysical Research: Solid Earth*, 124(8), 8584–8610. https://doi.org/10.1029/2019JB017684

Weng, H., & Ampuero, J.-P. (2020). Continuum of earthquake rupture speeds enabled by oblique slip. *Nature Geoscience*, 13(12), 817–821. https://doi.org/10.1038/s41561-020-00654-4

Xu, S., Fukuyama, E., & Yamashita, F. (2019). Robust estimation of rupture properties at propagating front of laboratory earthquakes. *Journal of Geophysical Research: Solid Earth*, 124(1), 766–787. https://doi.org/10.1029/2018JB016797